# ALTERNATIVE BUFFER LAYERS, DEVICE MODELING AND CHARACTERIZATION OF COPPER-INDIUM-DISELENIDE-BASED THIN-FILM SOLAR CELLS

By

CHIA-HUA HUANG

A DISSERTATION PRESENTED TO THE GRADUATE SCHOOL
OF THE UNIVERSITY OF FLORIDA IN PARTIAL FULFILLMENT
OF THE REQUIREMENTS FOR THE DEGREE OF
DOCTOR OF PHILOSOPHY

UNIVERSITY OF FLORIDA

2002

# ACKNOWLEDGMENTS

I want to express my deep appreciation to my advisor and the chairman of my Ph.D. committee, Professor Sheng S. Li, for his guidance and support of my research. I also wish to thank Professors Gijs Bosman, Arnost Neugroschel, and Timothy J. Anderson for serving on my supervisory committee.

I gratefully acknowledge the financial support of the National Renewal Energy Laboratory (NREL). I wish to thank Dr. Kannan Ramanathan of NREL, Dr. W.N. Shafarman of the University of Delaware, Siemens Solar Industries, and International Solar Electric Technology, Inc., for providing the samples for this study. I appreciatively acknowledge the use of AMPS-1D developed by Dr. S. J. Fonash of the Pennsylvania State University.

Special thanks are extended to Drs. Billy J. Stanbery, Chih-Hung Chang, Loren Rieth, Yun-Shan Chang, Jung-Chi Chiang, Jerome T. Chu, and Jung Hee Lee for their valuable discussions. I would like to extend my sincere appreciation to my colleagues, Lei Li Kerr, Suku Kim, Serkan Kincal, Junhee Moon, Lin Jiang, Jiyon Song, and Xuege Wang, in the laboratories for their assistance.

Finally, I am greatly indebted to my parents, S. L. Huang and Y. C. K. Huang, for their love, support and encouragement.

# TABLE OF CONTENTS

page

ACKNOWLEDGMENTS ii

ABSTRACT vi

CHAPTERS

1 INTRODUCTION 1

2 FUNDAMENTALS OF COPPER-INDIUM-DISELENIDE-BASED THIN-FILM SOLAR CELLS 7

- Overview 7
- Historical Perspective 8
- Technologies of $CuInSe_2$-based Solar Cells 10
  - Absorber Layers 11
    - Influence of gallium 13
    - Influence of sulfur 15
  - Buffer Layers 16
  - Junction Formation 17
  - Window Layers 19
  - Back Contact Layers 20
  - Substrates — Influence of Sodium 20
- High Performance $CuInSe_2$-based Solar Cells 21

3 EFFECTS OF BUFFER LAYER PROCESSING ON CIGS FILMS CHARACTERIZED BY DUAL BEAM OPTICAL MODULATION TECHNIQUE 29

- Introduction 29
- Simplified Theory for Reflection Mode DBOM Technique 31
- Experimental Details 36
  - Lifetime Measureemnt 36
  - Buffer Layer Processing 37
- Results and Discussion 39
  - Measurements of NREL Samples 39
  - Measurements of SSI and EPV Samples 42
- Conclusions 43

4 MODIFIED THEORY FOR REFLECTION MODE DUAL BEAM OPTICAL MODULATION TECHNIQUE ....62

Introduction .... 62
Modified DBOM Model for CIGS P-N Junctions Cells .... 63
Results and Discussion .... 68
Conclusions .... 69

5 FABRICATION OF COPPER-INDIUM-DISELENIDE-BASED SOLAR CELLS....76

Introduction .... 76
Photolithographic Process .... 76
Fabrication of Laboratory-Scaled CIS-Based Solar Cells .... 77

6 CURRENT-VOLTAGE AND SPECTRAL RESPONSE MEASUREMENT SYSTEMS ....79

Introduction .... 79
Current-Voltage Measurement Instrumentation and Procedures .... 81
  Current-Voltage Measurement Instrumentation .... 81
    Solar simulator and irradiance control .... 81
    Measurement plateform and temperature control .... 82
    Current-versus-voltage measurements .... 82
    Data acqusition and analysis .... 83
  Current-Voltage Measurement Procedures .... 83
Spectral Response Measurement Instrumentation and Procedures .... 84
  Spectral Response Measurement Instrumentation .... 84
    Monochromator and monochromatic light source .... 85
    Monochromatic light chopper .... 86
    Bias light source .... 87
    Spectral detector and sysnchronous detection instrumentation .... 87
  Spectral Response Measurement Procedures .... 88

7 DEVELOPMENT AND CHARACTERIZATION OF BUFFER LAYER FOR COPPER-INDIUM-DISELENIDE-BASED SOLAR CELLS ....94

Introduction .... 94
Processing .... 96
  Chemical-Bath-Deposition Conditions .... 96
  Device Fabrication .... 97
Characterization of CdS, (Cd,Zn)S, ZnS, and In(OH)$_x$S$_y$ Buffer Layers .... 97
  Compositional Analysis .... 97
  Optical Properties .... 101
Current-Voltage Characteristics of CIGS-Based Solar Cells with CdS, (Cd,Zn)S, ZnS, or In(OH)$_x$S$_y$ Buffer Layers .... 101
  CIGS-Based Cells with CdS or (Cd,Zn)S Buffer Layers .... 101

CIGS-Based Cells with ZnS Buffer Layers ........ 102
CIGS-Based Cells with $In(OH)_xS_y$ Buffer Layers ........ 103
Summary and Conclusions ........ 105

8 DEVICE MODELING AND SIMULATION OF COPPER-INDIUM-DESELNIDE-BASED SOLAR CELLS ........ 120

Introduction ........ 120
Simulation of Copper-Indium-Diselenide-Based Solar Cells ........ 122
Results and Disscusion ........ 123
Impacts of Graded Band-gap on Performance of CIGS Solar Cells ........ 123
Impacts of Inverted Surface Layer on Performance of CIGS Solar Cells ........ 126
Summary ........ 128

9 SUMMARY AND FUTURE STUDIES ........ 137
Summary and Conclusions ........ 137
Future Studies ........ 138

LIST OF REFERENCES ........ 141

BIOGRAPHICAL SKETCH ........ 149

Abstract of Dissertation Presented to the Graduate School
of the University of Florida in Partial Fulfillment of the
Requirements for the Degree of Doctor of Philosophy

# ALTERNATIVE BUFFER LAYERS, DEVICE MODELING AND CHARCTERIZATION OF COPPER-INDIUM-DISELENIDE-BASED THIN-FILM SOLAR CELLS

By

Chia-Hua Huang

August 2002

Chair: Sheng S. Li
Department: Electrical and Computer Engineering

The goal of this research is aimed at developing Cd-free alternative buffer layers and performing the device modeling and numerical simulations of optimized device structures and parameters for enhancing the performance of copper-indium-diselenide (CIS)-based thin-film solar cells. To facilitate the characterization of CIS-based cells a reflection mode dual beam optical modulation (DBOM) technique was developed for determining the excess carrier lifetimes in the CIS and $Cu(In,Ga)Se_2$ (CIGS) films. Additionally, the computer-controlled automatic current-voltage (I-V) and spectral response (quantum efficiency) measurement systems with *LabVIEW* programs for controlling the measurement procedures and data acquisition were developed.

Several buffer-layer materials including CdS, (Cd,Zn)S, ZnS, and $In(OH)_xS_y$ deposited by the chemical-bath-deposition (CBD) process were investigated for the cell fabrication. Among the CIS-based cells with CdS, (Cd,Zn)S, ZnS, or $In(OH)_xS_y$ buffer layers studied in this research, the CIGS/CdS cell gave the best performance. A higher short-circuit current density was obtained for the CIGS/ZnS cell than for the CIGS/CdS cell.

A comprehensive study of the device modeling and simulation of CIGS solar cells with an emphasis on the band-gap engineering of the CIGS absorber layers was carried out. The device physics and performance parameters of the CIGS absorber layers with different band-gap profiles were analyzed. Additionally, the dependence of performance parameters of the CIGS cells on the material parameters of the Cu-poor surface defect layer in the CIGS absorber layers was investigated.

A reflection mode DBOM technique was developed to investigate the effects of various CdS-buffer-layer processes on the excess carrier lifetimes in the CIGS films. To explain these DBOM results, a modified analytical DBOM formulation for the carrier lifetime of CIGS p-n junction cells was derived.

To sum up, the major contributions of this research include an assessment of Cd-free buffer layers for improving the performance of CIS-based cells, analysis of impacts of band-gap profiles and junction parameters on device performance, and development of the computer-controlled device characterization systems for measuring the performance parameters of the cells. The optimization of buffer-layer process and enhancement of junction quality by laser annealing process to further improve the performance of CIS-based cells are suggested for future studies.

# CHAPTER 1
# INTRODUCTION

Worldwide energy consumption is rising year after year. Most of the energy comes from sources of petroleum, natural gas, windmill, geothermal, fossil fuel, and nuclear power generation. These types of power generation systems are polluting, costly, or exhausted after all. Therefore, it is necessary to seek a renewable energy source to replace these power generation systems for the protection of our natural environment and future use. The sun has been radiating energy for over 500 million years and is expected to continue for at least another 50 million years. The photovoltaic (solar) energy conversion is an excellent candidate for the renewal energy source because it is free, clean, inexhaustible, uninterruptible, and nonpolluting. Solar cells, which use the internal photovoltaic effect in a semiconductor, are capable of providing electricity directly from the sun for a wide variety of applications with the advantage of long-duration power generation at a lower operating cost.

In recent years, a great deal of efforts has been devoted to the development of various low-cost, high-efficiency, and high-stability solar cells for both terrestrial and space power generation as well as for applications in consumer electronics. Cost and conversion efficiency are always the two key factors to determine the compatibility of a solar cell. The thin-film solar cells give the best hope for obtaining photovoltaic devices with the goals of both high efficiency and low cost. Copper indium diselenide ($CuInSe_2$ or CIS) and copper indium gallium diselenide ($CuIn_{1-x}Ga_xSe_2$ or CIGS) films, which have been of much interest as photovoltaic materials in recent years, are the most promising thin-film materials among all thin-film solar cell technologies for achieving these goals. The interest arises primarily for the following reasons: The direct band-gap energy of around 1.02eV and 1.14eV for CIS and CIGS, respectively, at 300°K is nearly ideal for a photovoltaic device operating in the solar spectrum. So far, there is no reported photon degradation of CIS solar cells due to good thermal stability. It can absorb the solar spectrum within a few micrometers with its high optical absorption coefficient. Moreover, the best CIGS thin-film solar cell has reached a maximum AM1.5G conversion efficiency of 18.8%. However, further optimization of the device performance could be greatly accelerated with a better understanding of some fundamental issues such as buffer layer processing, alternative buffer layers, and band-gap engineering within the absorber layers. For example, the open-circuit voltage of the CIS solar cells depends on the minority carrier lifetimes in the CIS films. In this research, we present a contactless diagnostic technique using the reflection mode dual beam optical modulation (DBOM) method to investigate the effects of buffer layer processing on the excess carrier lifetimes of CIS and CIGS absorber layers. The impact of alternative buffer layers on the device performance has been carried out in this research.

The scope of this research includes the studies of excess carrier lifetimes in CIS or CIGS films by using a contactless reflection-mode DBOM technique, development of various buffer layers for the CIS-based solar cells, fabrication of CIS-based solar cells, characterization of CIS-based solar cells by using current-voltage (I-V) and spectral response measurements, device modeling and numerical simulation of CIS-based solar cells. The main objectives include the following: (1) development of a new contactless reflection mode DBOM technique for mapping and determining the excess carrier lifetimes in the CIS and CIGS films for use as a quality control and processing evaluation tool in the fabrication of CIS and CIGS solar cells, (2) development of alternative buffer layers for the CIS-based solar cells, (3) development of a computer- controlled automatic measurement system for the characterization of dark- and photo-I-V and spectral response (QE) in the CIS-based solar cells, and (4) device modeling and simulation of CIS-based solar cells by employing the band-gap engineering and junction parameters to achieve optimal cell structures and device performance.

Chapter 2 summarizes the historical perspective, fundamental understanding, and present knowledge of CIS-based solar cells. Some critical and controversial issues such as the formation of electronic junction, the role of chemical-bath-deposition (CBD) of CdS buffer layers, and the role of intrinsic ZnO layer are still not fully understood. An overview of these issues is presented in this chapter. Additionally, the function and role of each component layer in the CIS-based solar cells are discussed. Furthermore, the approach of achieving high-performance CIS-based solar cells using tandem-cell structure is also given.

In Chapter 3, a reflection mode DBOM technique developed for the characterization of effective excess carrier lifetimes in the CIS and CIGS films deposited on Mo-coated soda-lime glass substrates is presented. This method utilizes the optical modulation of the reflected beam intensity of an infrared (IR) probe beam ($h\nu < E_g$)

modulated by a visible laser pump beam ($h\nu > E_g$) via free carrier absorption in the CIS and CIGS films. A simplified theoretical expression relating the change of modulated IR probe beam intensity ($\Delta I/I$) to the effective excess carrier lifetimes has been derived for the CIS device structure without consideration of the p-n junction in extracting the effective excess carrier lifetimes from the reflection mode DBOM measurements. In addition, the investigation of various CdS buffer-layer processes such as chemical bath deposition (CBD), metalorganic chemical vapor deposition (MOVCD), and sputtering process on the excess carrier lifetimes in CIGS films by using DBOM technique shows a significant increase in the DBOM signal ($\Delta I/I$), which is related to the change of free carrier absorption and the excess carrier lifetimes in the CIGS films after the buffer layer processing. Moreover, impacts of the intermediate surface treatments such as sulfur- and cadmium-partial electrolyte treatments, DI water rinsing, and argon (Ar) plasma cleaning on the excess carrier lifetimes of CIGS films were investigated as well.

In Chapter 4, an analytical DBOM model for the CIGS p-n junction cell is presented. The space charge region between the p-type CIGS film and the n-type CdS layer is taken into account in this modified model. Using continuity equations with boundary conditions, the expression which contains the functional dependence of DBOM signal $\Delta I/I$ on the parameters such as excess carrier lifetimes, diffusion length, depletion layer width, and surface/interface recombination velocities is derived to account for the observed DBOM signals described in Chapter 3.

In Chapter 5, the fabrication process of CIS-based solar cells is described. Both the detailed photolithographic process and simple process for the fabrication of CIS-based solar cells are given.

Chapter 6 describes the design and construction of a current-voltage (I-V) and spectral response (QE) measurement system for device characterization of the CIS-based solar cells. The selection and features of each component used in the measurement systems are discussed. The detailed procedures for an accurate measurement of CIS-based solar cell parameters are presented.

Chapter 7 presents the development and characterization of alternative buffer-layer materials such as ZnS, (Cd,Zn)S, and $In(OH)_xS_y$ for the CIS-based solar cells. The buffer layer materials of CdS, (Cd,Zn)S, ZnS, or $In(OH)_xS_y$ were deposited on the soda-lime glass substrates, CIGS, or $Cu(In,Ga)(Se,S)_2$ (CIGSS) thin films by the chemical-bath-deposition (CBD) process. The compositions of the deposited films were analyzed by the x-ray photoelectron spectroscopy (XPS) and auger electron spectroscopy (AES). Both the CIGS and CIGSS samples deposited with the CdS, (Cd,Zn)S, ZnS, or $In(OH)_xS_y$ buffer layers by the CBD process were fabricated into solar cells. The current-voltage (I-V) characteristics of these cells with the alternative buffer layers were measured, and the results were compared to the cells deposited with the CBD CdS buffer layers. The results show comparable performance among these cells, and further optimization of the deposition conditions could improve the performance of the CIS cells deposited with the alternative buffer layers.

The incorporation of Ga in CIS films is considered as a crucial factor in improving the performance of CIS-based solar cells. By varying the Ga content spatially within the absorber layers of CIGS solar cells, the technique of band-gap engineering can be applied to the CIGS solar cells to enhance the carrier collection and reducing the carrier recombination, and hence improves the device performance. On the other hand, until now the mechanisms responsible for the formation of electrical junction in the CIS-based solar cells are still not quite understood. In this research, the effects of band-gap engineering and junction parameters on the device performance were investigated by means of device modeling and simulation. The results and discussion are presented in Chapter 8.

Finally, Chapter 9 gives a summary and future direction for the fabrication of low-cost and high-efficiency CIGS thin-film solar cells.

# CHAPTER 2
# FUNDAMENTALS OF CIS-BASED SOLAR CELLS

## Introduction

As a simple definition, solar cells (photovoltaic cells) are semiconductor devices, which convert the energy of incident photons from sunlight into electric power. The incident photons with energy greater than the band-gap energy of the semiconductor will generate electron-hole pairs in a solar cell. With the optical absorption coefficients as high as $10^5$cm$^{-1}$ for the CIS material, the optical absorption depth is around 0.1μm in the CIS absorber layers. Thus, most of the electron-hole pairs are generated within the space charge region (SCR) of the CIS cells. These photo-generated carriers are swept by the built-in electric field from the SCR and are then collected at the contact electrodes. For the photo-generated carriers in the n- and p- quasi-neutral regions (QNR), they are transported by diffusion into the SCR and then collected at contact electrodes. Thus, the design of a low-cost, high-efficiency CIS solar cell requires a comprehensive investigation of optical, transport, and electrical properties of CIS absorber layers.

With the desirable properties of high optical absorption coefficients and direct band gap, the CIS-based thin-film solar cells have drawn much attention due to their potential for the fabrication of low-cost, high-efficiency, and high stability thin-film photovoltaic devices. One of the key advantages for the CIS cells is that the CIS- based material system offers the tunable band-gap energy and lattice parameters by alloying

CIS with gallium and/or sulfur to better match the solar spectrum and to be compatible with common window materials such as (Cd,Zn)S, ZnO, and indium tin oxide (ITO). Material availability at low cost can also be achieved along with a compatible low-cost substrate. Furthermore, n- and p-type material can be produced with excellent optical and electrical properties. Additional advantages of CIS-based solar cells include the long-term stability and radiation hardness.

## Historical Perspective

S. Wagner et al. reported the first CIS solar cell using a single crystal with a conversion efficiency of 12.5% in 1974 [1]. In 1976, the first thin-film CIS/CdS solar cell achieved a conversion efficiency of 6.6% [2]. In 1981, a major breakthrough reported by the Boeing Corporation demonstrated a thin-film solar cell of 9.5% efficiency using the polycrystalline CIS deposited by the elemental co-evaporation technique with a bi-layer structure of high- and low-resistivity CIS films [3]. This was soon followed in 1982 by a CIS cell with n-type $Zn_xCd_{1-x}S$ as a replacement of CdS exceeding 10% efficiency [4]. The method developed by the Boeing Corporation for the deposition of bi-layer CIS is the well-known "Boeing bi-layer process." The bi-layer CIS cell structure is illustrated in Figure 2-1. In contrast to the device structure with thick CdS layers (~3μm) of undoped and doped CdS employed by the Boeing Corporation, as illustrated in Figure 2-2 a novel CIS cell structure consisting of a thin undoped CdS layer and a conducting ZnO layer was first proposed to increase the photocurrent resulting from the enhancement of short-wavelength response in 1985 [5], which led to the standard structure of the present-day CIS-based solar cells. This device structure has resulted in a significant improvement in performance for the CIS-based solar cells. Incorporation of Ga or S in the CIS to improve the open-circuit voltage of the cells by increasing the band-gap energy was started in the late 1980s [6] and the early 1990s [7]. A new approach, which is different from the Boeing bi-layer process, for the deposition of CIS films using the selenization of stacked metal layers in $H_2Se$ was reported, which achieved an active-area 14.1% efficiency in 1988 [8]. In order to further realize the potential of CIS-based solar cells, in recent years the research efforts have been dedicated to the improvement of conversion efficiency in areas such as refining the deposition process for absorber layers, alloying CIS with Ga and/or S within the absorber for the band-gap engineering, improving the absorber quality, searching for the new alternative buffer layers with wider band-gap, enhancing the optical and electrical properties for the transparent conductive oxide (TCO) layers, and better understanding of the electronic and defect properties of the bulk materials and interface between the absorber and window layers. The device structure and deposition techniques of the present CIS-based solar cells are illustrated in Figure 2-3. The absorber layers, CIS or CIGS, are typically deposited by the physical vapor deposition (PVD) process on the soda-lime glass (SLG) substrates coated with sputtered molybdenum using the Boeing bi-layer process [4], three-stage process [9], or selenization process. Thin buffer layers such as CdS, ZnS, or $In(OH)_xS_y$ are then deposited by the chemical-bath-deposition (CBD) process. Following the CBD process, both the thin undoped ZnO layers (i.e., intrinsic ZnO layer) and transparent conductive oxide (TCO) layers such as ZnO films doped with Al, Ga, B, or F are deposited by the sputtering process. The films of $MgF_2$ are served as the anti-reflection layers for the CIS cells.

Most recently, CIGS solar cells with a device structure of soda-lime glass substrate/Mo/CIGS/CdS/ZnO have achieved an 18.8% conversion efficiency AM1.5G [10] and 21.5% efficiency under a concentrated illumination of 14 suns [11]. A summary for the best efficiency of CIS-based solar cells is given in Table 2-1. The factors influencing the remarkable improvements in the CIS-based solar cells are summarized as follows: (a) the addition of Ga in CIS films not only results in the increase of band-gap but also allows the band-gap engineering for the cell structure to improve the cell performance, (b) the replacement of the thick CdS layer deposited by the evaporation method with a combination of the thin chemical-bath-deposited CdS layer and wide-band-gap ZnO layer improves the junction quality and photo response in the short-wavelength region, and (c) the replacement of the sodium-free glass substrates by the sodium-contained glass substrates allows the diffusion of Na from the substrates through the Mo layers into CIS-based films during the subsequent deposition process to modify the structural and electrical properties of absorber layers. In addition, the device-quality absorber films deposited by the bi-layer process or three-stage process are attributed to the incorporation of both the Cu-rich layers and Cu-poor surface layers during the deposition process to achieve the improved electrical junction, adequate morphology, and satisfactory optical and electrical properties.

## Technologies of $CuInSe_2$-Based Solar Cells

As illustrated in Figure 2-3, a typical CIS-based solar cell consists of the CIS-based films as absorber layers, CdS buffer layers, ZnO films as the top-contact layers, Mo films as the bottom-contact layers, and substrates for the support of the thin-film cells.

The basic functions and properties of each component of CIS-based solar cells are depicted below.

**Absorber Layers**

Without a doubt, the CIS or CIGS absorber layer is the most critical element in the CIS-based solar cells. With three (i.e., Cu, In, and Se) or even five (i.e., Cu, In, Ga, Se, and S) elements involved in the chalcopyrite semiconductors, the material system of the I-III-$VI_2$ semiconductor, namely Cu $(In_{1-x}Ga_x)(Se_yS_{1-y})_2$, is very complex in terms of its electrical, optical, and structural properties. Based on the quasi-binary phase diagram of CIS, the existence range of single-phase CIS is extremely small at room temperature. Thus, a wide variety of compounds can possibly be created during the deposition process. Although substantial knowledge of the fundamental material properties for the CIS, CGS, and CIGS has been gained in recent years, so far the direct correlation between the deposition conditions and resulting device performance is still not completely understood.

With its high optical absorption coefficients and direct band gap, the $CuInSe_2$ becomes a natural choice for the application in the thin-film solar cells. Based on a simple calculation of light absorbed in a semiconductor, the irradiance $E(x,\lambda)$ decays exponentially with depth $x$ from the surface of the semiconductor can be expressed by

$$E(x,\lambda) = E_0 e^{-\alpha(\lambda)x} \quad (2.1)$$

where $E_0$ is the incident irradiance at the surface of the semiconductor, $\lambda$ is the wavelength of incident light, and $\alpha$ is the optical absorption coefficient of the semiconductor. For the CIS with an absorption coefficient as high as $10^5 cm^{-1}$, half a micron meter of CIS film can absorb more than 99% of incident photons. However, due to properties of polycrystalline CIS-based thin-film solar cells, typical thickness of the absorber layers used in the CIS cells is in the range of 1.5 to 2.5μm. The reasons for using the thickness of around 2μm the CIS absorber layer can be explained below. First, the roughness of CIGS films is about 0.3-0.4μm in spite of the total film thickness [12]. When the film thickness is down to 0.5μm, which is comparable to the roughness of the film, the shunt path can be easily created and can degrade the cell performance. Moreover, with a typical diffusion length of around 2μm for the CIGS, thinner CIGS films could result in a higher recombination rate at the back interface between the CIGS and Mo layers, and hence the cell performance is deteriorated. Thus, efforts of refining the deposition process to obtain a smooth film surface and introducing the back surface field to reduce the back surface recombination are being made to reduce the absorber thickness, which could further reduce the cost of manufacturing CIS-based solar cells.

The electrical conductivity of the CIS-based films can be prepared in either n- or p-type. Typically, the CIS-based films used in the solar cells have an overall p-type conductivity with a net carrier density in the order of around $10^{16}$cm$^{-3}$. It is well known that the electrical conductivity of CIS films is controlled by the intrinsic defects via the compensation between the donor-like and acceptor-like defects depending on the atomic ratio of [Cu]/[In] and [Se]/([Cu]+[In]). Selenium-rich and selenium-poor CIS films usually show the p-type and n-type conductivity, respectively. The defect of Se vacancy ($V_{Se}$) is considered as the dominant donor in the n-type material and as the compensating donor in the p-type CIS films. On the other hand, the p-type CIS films can be obtained by depositing more copper than indium in the films. Similarly, the n-type CIS films can be obtained by the reverse process.

By incorporation of Ga and/or S in the CIS films, $Cu(In_{1-x}Ga_x)(Se_yS_{1-y})_2$ provides a high level of flexibility in the CIS-based cell fabrication for improving the cell performance and a possibility of forming CIGSS absorber layers with band-gap energies varying from 1.04eV (e.g., $CuInSe_2$) up to 2.4eV (e.g., $CuGaS_2$) allowing the optimal band-gap design and application of tandem-cell structure.

**Influence of gallium**

In manufacturing the CIS solar cell modules, higher open-circuit voltage ($V_{OC}$) and lower short-circuit current ($J_{SC}$) are preferred for the minimization of interconnection loss. Adding Ga in the CIS can increase the band-gap energy of CIGS films and hence increases the $V_{OC}$ in the CIGS cells. In addition, the CIGS films with an optimum band-gap energy of 1.5eV matches the solar spectrum and can potentially achieve high conversion efficiency in CIGS cells.

Researchers have conducted extensive studies of the effects of Ga on the device performance of CIGS solar cells. The results showed that the $V_{OC}$ increases with increasing Ga content in the CIGS films. However, the $V_{OC}$ does not increase proportionally with the content of Ga in CIGS cells. The short-circuit current decreases with the increase of Ga content in the CIGS films due to the lower absorption coefficients and the reduced absorption in the long-wavelength portion of the spectrum. The best $CuIn_{1-x}Ga_xSe_2$ solar cells are fabricated with a ratio of x=[Ga]/([Ga]+[In]) at around 0.25~0.3 corresponding to a band-gap energy of around 1.15 eV for the CIGS films. The conversion efficiency of CIGS cells starts to drop when the content of Ga exceeds 30% in the CIGS films. Although attempts to use the wide band-gap CIGS materials for the thin-film solar-cell modules were not totally successful, the incorporation of Ga in the CIS films is considered as a key factor for improving the conversion efficiency of CIS-based solar cells to near 20%. Moreover, the incorporation of Ga in the CIS films allows band-gap engineering within the absorber layers, which can significantly improve the CIGS cell performance. A detailed discussion of this issue will be presented in Chapter 8.

With a band-gap energy of 1.68eV, the $CuGaSe_2$ is considered as an excellent candidate for the top cell with the $CuInSe_2$ as the bottom cell for the fabrication of two-junction tandem cells. Research on using p-type $CuGaSe_2$ as the photovoltaic materials to make single-junction solar cells was first reported in 1977 [13, 14]. The best $CuGaSe_2$ solar cell, which used the single crystal $CuGaSe_2$, yielded a conversion efficiency of 9.7%, open-circuit voltage of 0.946V, short-circuit current of 15.5mA/cm$^2$, and fill factor of 66.5% [15]. The polycrystalline $CuGaSe_2$ solar cells with a cell structure of soda-lime glass substrate/Mo/$CuGaSe_2$/CdS/ZnO achieved an active-area conversion efficiency of 9.32% and an open-circuit voltage of 0.87 V in 1997 [16]. Compared to a 6.2% efficiency $CuGaSe_2$ fabricated in 1991 [17] the improvements are attributed to a slightly Ga-rich absorber composition, the use of Na-containing glass substrates, and an optimal deposition temperature of CdS buffer layer for the $CuGaSe_2$ absorbers [18]. Using CGS as the top cells in the tandem cell structure, the efficiency of CGS cells must reach around 15% in order to achieve a 25% efficiency tandem cells. In order to realize this goal, some critical issues must be addressed. Generally, the open-circuit voltage of CIS and CIGS solar cells can be described by the equation of $V_{OC} \approx E_g/q–0.5V$ where $E_g$ is the band-gap energy of the absorber and q is the electronic charge [18]. If the open-circuit voltage of $CuGaSe_2$ solar cells also follows this relation, an open-circuit voltage of 1.2V should be obtained for the $CuGaSe_2$ solar cells. However, CGS solar cells usually have a lower open-circuit voltage than the expected value. Another problem for the CGS solar cells is that the net hole concentration in $CuGaSe_2$ films is usually around $10^{18}$ $cm^{-3}$ and hence the width of the space charge region in the absorber side is very small. Thus, the diffusion length for the minority carriers in the absorber must be sufficiently long to obtain a high carrier collection efficiency. To resolve this problem, a reduced net hole concentration to $10^{16}cm^{-3}$ in the CGS absorber must be achieved to extend the depletion width in the absorber layer and to improve the carrier collection [19].

**Influence of sulfur**

In order to achieve a maximum conversion of the solar energy into electricity for terrestrial applications, the optimal band-gap of the semiconductor used in the solar cells is about 1.5eV [20]. The $CuInS_2$ thin film, one of the ternary chalcopyrite compounds, with high absorption coefficients and direct band-gap energy of around 1.5eV is an excellent candidate for the low-cost thin-film solar cells. For the concern of friendly environment and commercial production, the use of sulfur and its compound is preferred. Due to the low conductivity of Cu-poor $CuInS_2$, $CuInS_2$ solar cells typically use Cu-rich preparation. During the deposition of Cu-rich $CuInS_2$, the secondary phase, namely $Cu_{2-y}S$, is also created at the same time. This secondary phase needs to be etched out in the solution of KCN in order to obtain the device-quality films. Up till now, the $CuInS_2$ solar cells with CBD CdS or $In_x(OH,S)_y$ buffer layers have demonstrated a conversion efficiency of about 12% and 11.4% [21, 22], respectively. However, the performance of both structures is limited by a moderate open-circuit voltage ($V_{OC}$≈720-735mV), which is lower than expected [23].

**Buffer Layers**

CdS buffer layers were initially considered as an n-type heterojunction partner with a good lattice match to the p-type CIS or CIGS films used in the CIS-based solar cells. The evolution of buffer layers for the CIS-based solar cells from the thick CdS layers consisting of both high- and low-resistivity layers deposited by using high vacuum evaporation technique to the thin buffer layers deposited by the chemical-bath-deposition (CBD) method in the past decade has led to the significant improvement in the device performance of CIS-based solar cells. So far, the best CIGS solar cells still use a thin buffer layer of CdS film, which is deposited by CBD method between the CIGS films and ZnO layers. Typical CBD CdS films are grown from an ammonia-contained chemical solution with Cd ions and thiourea at a temperature of around 80°C. The benefits of CBD CdS for the CIGS solar cells include both the material properties of CdS and the unique features of the deposition process. The CdS buffer layers were suggested to provide a better band alignment of the device. The properties of CIGS surface are modified by the intermixing at the CIGS surface and/or diffusion of Cd ions from the bath solution into the CIGS films substituting Cu ions during the deposition process. Thus, an effect of n-type doping on the surface region of CIGS films is established. The passivation of CIGS surface and removal of the natural oxide from the CIGS surface that occurred during the deposition process result in a low surface recombination velocity and a better interface quality. In addition, the rough CIGS surface is uniformly covered by the CBD CdS films, providing a protection against the potential damage and oxidation from the following sputtering deposition process and avoiding the shunt path created between the CIGS and the conducting layers. Thus, the CBD CdS buffer layer plays a very important role in the fabrication of CIS-based solar cells.

Due to the toxicity of Cd and handling of material waste associated with the use of CBD CdS in the CIS-based solar cells, the research efforts are motivated to search for the alternative buffer-layer materials. In addition, the replacement of CdS with wider band-gap materials can further improve the photo-response of cells in the short-wavelength region, and hence the short-circuit current density can be improved. However, a different mechanism of modifying the absorber surface might be anticipated for the alternative buffer layers. A detailed discussion of alternative buffer layers for the CIS-based solar cells is presented in Chapter 7. From the viewpoint of manufacturing CIS-based solar cells in the in-line fabrication system, the vacuum deposition process for the deposition of buffer layers is definitely more favorable than the wet process such as chemical bath deposition. The development of vacuum process for this purpose is still an active area of research. Other possible option includes the complete elimination of the buffer layers for the buffer-layer free CIS-based solar cells [24].

### Junction Formation

At first, an abrupt hetero-junction was considered to form in the device structure of p-type CIS/n-type CdS solar cells. However, several different junction models have been proposed with a certain level of discrepancy. Up to the present day, the exact nature of the electronic junction still remains an unsettled issue.

In 1993, Schmid *et al.* proposed a model of chalcopyrite/ defect chalcopyrite heterojunction between the p-type bulk CIS and the n-type In-rich surface layer [25]. Based on the in-situ photoemission measurements, it is shown that an n-type In-rich surface layer existed on the as-deposited CIS films. This phase-segregation layer was identified as an order vacancy compound (OVC) with the band-gap energy of 1.3eV and tentatively assigned as the stoichiometry $CuIn_2Se_{3.5}$ or $CuIn_3Se_5$. However, the existence of OVC on the CIGS films has not been confirmed by structural characterizations.

Another viewpoint for the CIS junction model is the Fermi level pinning by the electronic states at the CIS surface. With the dangling bond of missing Se at the surface of CIS, the shallow surface donors of positively charged vacancies $V_{Se}$ result in the band bending of CIS at the surface, and hence n- type inversion occurs. Under air exposure or annealing, these surface charges are neutralized and the n-type inversion disappears. However, the subsequent CBD process is expected to remove the oxidation created during the air exposure or annealing and re-establishes n- type inversion at the interface between the CdS and the CIS films.

On the other hand, efforts have been directed towards understanding the mechanisms responsible for the performance improvement of CIS-based solar cells when the CBD CdS buffer layer is deposited on the CIS or CIGS absorber layers. It has been observed that intermixing occurred around the interface between the CdS and CIGS [26]. Direct evidence of Cd diffusion into CIGS films during the CBD process was also reported [27]. Furthermore, it has been suggested that substitution of Cd ions for Cu vacancy sites producing substitutional donors for the CIGS films with the treatment of Cd-partial electrolyte. An n-type inversion layer at the surface of CIGS films was created by the Cd doping. Thus, the electronic junction was suggested to form within the CIGS films.

### Window Layers

In the CIS-based solar cells, a high-resistivity/low-resistivity bi-layer of ZnO is generally deposited on top of the CdS buffer layer by sputtering process. The high-resistivity ZnO layers (i.e., undoped ZnO, intrinsic ZnO, i-ZnO) with a thickness of around 50nm are typically deposited by rf-magnetron sputtering process. The transparent and conductive oxide layers, namely ZnO layers doped with Al or B (i.e., ZnO:Al or ZnO:B), are then deposited and served as the top electrodes of CIS-based solar cells.

A typical i-ZnO layer with conductivity of less than $10^{-4}$ $\Omega$-cm$^{-1}$ yields the best performance. However, the role of i-ZnO layer in CIS-based solar cells is still not well understood. Recently, the function of i-ZnO layer is explained as that this intrinsic layer together with buffer layer prevent the non-uniformities of electrical properties within the entire area of the cell from dominating the open-circuit voltage [28]. Since the top contact layer of CIS-based solar cells requires the properties of both high conductivity to reduce electrical loss and high transparency to minimize the absorption of photons. The wide band-gap materials such as heavily doped ZnO layers with a thickness in the range of 0.35-0.5 μm are suitable for this purpose. The ZnO:Al layers with a resistivity of less than $5\times10^{-4}$ $\Omega$-cm and a transmittance of greater than 80% in the visible range of the spectrum are considered acceptable for the present-day CIS-based solar cells.

### Back Contact Layers

The molybdenum (Mo) layers with a thickness of around 1 μm deposited by d.c.-magnetron sputtering process are used in the bottom contact layers for the CIS-based solar cells. With the exclusive properties of low contact resistance to the CIS and CIGS, relative stability at the processing temperatures (400-600°C), and resistance to react with Cu, In, and Ga, the Mo is the common metal used in the back contacts of CIS-based solar cells.

Followed the deposition of CIS or CIGS on the Mo-coated glass substrates, an interfacial $MoSe_2$ layer between the absorbers and Mo layers has been identified. This layer structure of $MoSe_2$ was suggested to have a band-gap energy of about 1.4eV with a thickness of around 0.1 μm. Besides that the wide-band-gap $MoSe_2$ layer can be served as the back surface field in the CIS-based solar cells to enhance the carrier collection, the $MoSe_2$ layers are considered to improve the adhesion of CIS films to the Mo contacts and to form good ohmic contacts.

### Substrates — Influence of Sodium

The early CIS solar cells generally used the molybdenum-coated alumina or Na-free glass as substrates. Lately, the soda-lime glass substrates were employed in the CIS-based solar cells primarily due to its low cost. In 1992, it was found that $CuInSe_2$ films deposited on the soda-lime glass substrates offer the properties of large grains, strong <112> orientation, and low porosity with improved device performance such as higher open-circuit voltage and fill factor [29]. These observed improvements were attributed to the optimum match of the thermal expansion coefficients between the soda-lime glass substrates and the CIS films, and the positive impacts of out-diffusion of Na from substrates on the grain growth, film morphology, and electronic conductivity. It is obvious that the benefits of using soda-lime glass substrates not only for the low-cost but also in the performance improvement. However, the interpretation of the beneficial effects is still under debate.

An important feature of the CIS-based thin-film solar cells is that the CIS absorber layers can be grown on the flexible substrates such as stainless steel, foil, or polymer substrates. The CIGS solar cells deposited on the stainless steel substrates have achieved a conversion efficiency of 17.4% AM1.5G [10].

### High Performance $CuInSe_2$-Based Solar Cells

As mentioned previously, the electron-hole pairs are generated only when the energy of incident photons are greater than the band-gap energy of semiconductors in the solar cells. Besides that the incident photons provide sufficient energy to produce electron-hole pairs, a considerable amount of photon energy in excess of the band-gap energy of semiconductors is typically dissipated into heat in the solar cells without contributing to the conversion of electric power. Moreover, the incident photons with energies less than the band-gap energy of the semiconductor will be dissipated as the lattice heat in the solar cells. In order to reduce these fundamental power losses, tandem (multi-junction) cell structure provides a drastic improvement in the conversion efficiency of solar cells and uses the sunlight spectrum more effectively. The idea of tandem solar cells was first proposed by E.D. Jackson in 1955 [30]. It employs a stack of single-junction solar cells with the larger band gap cells on top of the smaller ones to efficiently convert the photons in different wavelength regions of the solar spectrum into electricity. A similar concept to effectively use the sunlight spectrum was also described by D. Trivich and P.A. Flinn in the same year [31].

The tandem solar cells can be fabricated by using either a mechanically stacked cascade or a monolithic cascade approach. A two-junction four-terminal mechanically stacked cell is composed of separately fabricated individual cells bonded together with transparent adhesive. A two-junction two-terminal monolithic cell consists of the active photovoltaic junctions together with a shorting junction (intercell ohmic contact) that serves as an electrical connection of the individual cells. The key advantages of the monolithic structure include that it is simple to incorporate the two-terminal devices into modules and potentially have very low cost/kW-hr [32]. The physical cell-cascade configurations have a significant influence on the approaches of fabrication procedures and material growth, and the conversion efficiency and cost of the multi-junction solar cells.

Reports on the design and theoretical studies of tandem (multi-junction) solar cells include investigations of two-junction monolithic or mechanically stacked cascade cells, multiple junction cells, material considerations, thermodynamic approaches, cells under different spectra, cells at different temperatures, cells under different sun light concentrations, and various aspects related to cell performance such as top-cell thickness, subcell connectivity, junction temperature, and top cell quantum efficiency [33-46]. In addition, the computer simulation programs such as ADEPT [47-48] and AMPS [49-50] were developed to analyze and design the tandem solar cells. For terrestrial applications, the optimal band-gap-energy combination of a two-junction tandem solar cell is in the range of 1.6-1.8 eV for the top cell and 0.9-1.2 eV for the bottom cell [33-35].

Although the extensive studies of tandem cells in various III-V material systems have been reported, the studies of tandem cells using polycrystalline I-III-VI material systems (e.g., CGS/CIS) are still very limited. Several two-junction tandem cells using CIS materials as the bottom cells were reported in the literatures [51-58]. In the case of mechanically stacked 4-terminal tandem cells, Meyers *et al.* reported a polycrystalline CdTe/CIS tandem cell with an efficiency of 9.9% [51], and Mitchell *et al.* demonstrated a 15.6% efficient semi-transparent thin-film *a*-Si:H alloy (TFS)/CIS tandem cell and a 12.3% aperture efficiency TFS/CIS module in 1988 [52]. All measurements were under the conditions of AM1.5G, 100 mW/cm$^2$, and 25°C. For space application a GaAs/CIS mechanically stacked tandem cell with efficiency of 23.1%, AM0, one sun, 28°C was reported in 1990 [53]. On the other hand for the monolithic two-terminal tandem solar cells, the Institute of Energy Conversion (IEC) of the University of Delaware reported a 3% efficiency CdTe/CIS tandem cell in 1984 [54] and a 5.8% efficiency *a*-Si:H/CIS tandem cell in 1988 [55]. $AgInS_2$ with a band gap energy of 1.87eV and lattice constant $a_o$ = 5.83Å was considered as an excellent match to CIS as the top cell material of tandem solar cells [56-57]. However, only n-type $AgInS_2$ has been reported so far. The $CuGaSe_2$ (CGS) with a band-gap energy of 1.68eV and CIS with a band-gap energy of 1.04eV are an ideal combination for the low-cost two-junction tandem solar cells. The CGS/CIS tandem solar cells with a theoretical efficiency of 33.9% was predicted as early as 1984 [58], but no experimental effort on the CGS/CIS tandem cells has been reported in the literature.

The tunable band-gap energy and outstanding material properties of chalcopyrite material system are suitable for the tandem-cell structure. However, some challenging issues of using CIS-based materials for the realization of the tandem cell structure still need to be addressed. In order to achieve a 25% efficiency tandem cell, the wide band-gap ($E_g$≈1.6-1.8eV) top cell with efficiency in the range of ~15% must be developed. For the manufacture of monolithic tandem cells, the low-temperature processes for the deposition of the top cells and tunnel junctions are required. In addition, the shorting junction or a novel structure designed for the interconnection between the top and bottom cells must be developed for the monolithic tandem-cell structures. In brief, the development of CIS-based tandem cell is not an easy task but is worthy of research efforts to explore its potential for the high-efficiency low-cost thin-film tandem cells applications.

Table 2-1. The performance parameters of the best CIS-based solar cells

| Absorber | $E_g$ | Conversion Efficiency | $V_{OC}$ | Ref. |
|---|---|---|---|---|
| $CuInSe_2$ | 0.95eV | 13.2% (total area) | 484mV | [59] |
| $CuInSe_2$ | 1.02eV | 16.1% (active area) | 519mV | [60] |
| $CuInS_2$ | 1.50eV | 11.4% (total area) | 729mV | [61] |
| $CuGaSe_2$ | 1.68eV | 9.3% (active area) | 870mV | [16] |
| $Cu(In_{1-x}Ga_x)Se_2$ | 1.15eV | 18.8% (total area) | 678mV | [10] |
| $Cu(In_{1-x}Ga_x)Se_2$ (14 suns) | 1.15eV | 21.5% (total area) | 736mV | [11] |
| $Cu(In_{1-x}Ga_x)(S_{1-y}Se_y)_2$ | 1.36eV | 13.9% (active area) | 775mV | [62] |

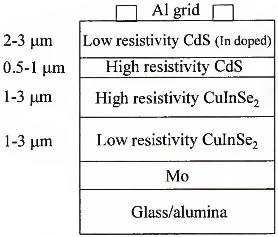
Al grid
2-3 μm
Low resistivity CdS (In doped)
0.5-1 μm
High resistivity CdS
1-3 μm
High resistivity $CuInSe_2$
1-3 μm
Low resistivity $CuInSe_2$
Mo
Glass/alumina

Figure 2-1. The early device structure of CIS solar cells developed by the Boeing Corporation.

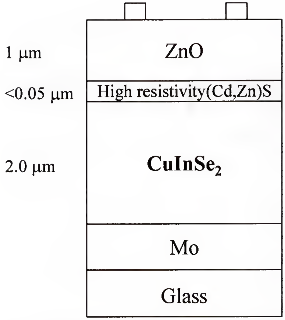

Figure 2-2. The device structure of CIS solar cells proposed by R.R. Potter *et al.* in 1985 for the improvement of photocurrent.

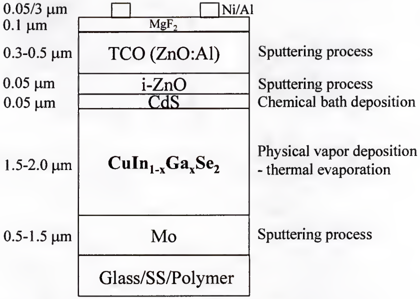

Figure 2-3. The present-day device structure of CIS-based solar cells.

# CHAPTER 3

# EFFECTS OF BUFFER LAYER PROCESSING ON CIGS THIN FILMS CHARACTERIZED BY DUAL BEAM OPTICAL MODULATION TECHNIQUE

## Introduction

$CuInSe_2$ (CIS) or $CuInGaSe_2$ (CIGS) thin film solar cells have achieved conversion efficiencies as high as 18.8% AM1.5G [10]. However, to accelerate the further optimization of the device performance, a detailed study and a better understanding of the effects of processing on the CIGS/CdS interface and CIGS film transport properties are needed.

Optimization of $CuInSe_2$ (CIS) or $Cu(In,Ga)Se_2$ (CIGS) thin-film solar cell requires the deposition of a thin CdS buffer layer between the CIS absorber layer and the ZnO window layer. A great deal of efforts have been devoted to better understanding the role of CdS buffer layers deposited by different processing techniques on the performance of CIS and CIGS cells. In order to understand why the chemical-bath-deposited (CBD) CdS buffer layer works so well on CIGS solar cells, a study of various CdS buffer layer processes on the excess carrier lifetimes and material characteristics of CIGS solar cells has been carried out. The CBD grown CdS layer is usually thick enough to completely cover the rough surface of CIS or CIGS absorber layers. Thus, a pinhole-free conformal coverage buffer layer is formed. Different buffer layer processes such as MOCVD and sputtering CdS processes are investigated and compared with CBD process. In addition, uncertainties remain as to whether the exchange reactions occurring at the interface of

CdS and CIGS region with Cd or S ions which chemically passivate the surface, the effect of water rinsing the surface of CIGS removing the soluble components [63], or combinations of these mechanisms affecting the excess carrier lifetimes in the CIGS films. It is shown that Cd binds easily on the surface of CIGS film [64]. Thus, CdSe and $CdIn_xSe_y$ are suggested to form and are responsible for graded interface structure [63]. The chemical modification of the CIGS absorber surface such as Cd- and S-partial electrolyte treatment, DI water rinsing treatment and Ar plasma cleaning treatment prior to CdS deposition are also investigated to study their effects on excess carrier lifetimes. Both the effects of annealing at 200°C after the intermediate treatments and MOCVD deposited CdS on as-deposited as well as after-intermediate-treated samples on excess carrier lifetimes of the CIGS films are discussed.

In this study, the reflection mode DBOM technique is employed to investigate the effects of different CdS buffer layer processings (i.e., CBD, MOCVD, and sputtering) on the properties of CIGS films [65]. The results show a significant increase in the DBOM signal ($\Delta I/I$) which is related to the change of the free carrier absorption and of the excess carrier lifetime in the absorber layer, after the buffer layer processing. Mapping of excess carrier lifetimes across the samples can be easily conducted by DBOM technique and it exhibits the substantial inhomogeneity of lifetime even for very high quality CIGS samples from various sources. Thus the capability of DBOM can be applicable to the quality assessment and process optimization for the CIGS films. This novel nondestructive optical technique provides a powerful means for assessing the quality of CIGS films, a vital requirement for the viable CIGS solar-cell manufacturing.

The reflection mode DBOM technique was applied to study the effects of CdS buffer layers deposited by the CBD, MOCVD, and sputtering processes on the excess carrier lifetimes in CIGS films. A detailed comparison of the DBOM data versus different processing, the measurement and mapping of excess carrier lifetimes in the CIGS films by the DBOM technique are presented. Considering the thickness of space charge region between n-type CdS and p-type CIGS as zero, the simplified reflection DBOM theory is employed to obtain the effective excess carrier lifetimes. A summary of the DBOM measurement results for CIGS films grown by National Renewal Energy Laboratory (NREL), Siemens Solar Industries (SSI), and Energy Photovoltaics, Inc. (EPV) using different growth techniques, deposited by different buffer layer processes, and treated by intermediate surface treatments (i.e., as deposited, DI water rinsed, Cd- and S-partial electrolyte treatment, and Ar plasma cleaned) is given in this chapter.

## Simplified Theory for Reflection Mode DBOM Technique

Since CIGS solar cells use thick Mo as backside ohmic contacts, a reflection mode DBOM technique has been developed for the measurement of excess carrier lifetimes in the CIGS films. The contactless DBOM technique is based on the modulation of the reflected intensity of an infrared (IR) probe beam by a visible pump beam which produces free carrier absorption in the CIGS film. The fractional change in the reflected intensity of the IR probe beam is directly proportional to the effective excess carrier lifetime in the CIGS films. Thus, the DBOM technique can be used to determine the excess carrier lifetimes in the CIGS films. It is also possible to perform depth profiling of the excess carrier lifetimes in the film by changing the wavelength (and hence the absorption depth in the film) of the pump beam.

Figure 3-1 shows the incident and reflected angles of the pump beam and probe beam in the CIGS device structure without p-n junction. The excess electron density, $\Delta n(x)$, generated by the pump beam in the CIGS layer can be obtained by solving the continuity equation for electrons and using the boundary conditions at the top ($x = 0$) and bottom interface ($x = t_b$) of the CIGS film, and the result yields

$$\Delta n(x) = \frac{\alpha\phi_0(1-R-T)\cos\theta_3}{D_n(\alpha^2 - \frac{1}{L_n^2})}\left(C_1 e^{\frac{x-t_b}{L_n}} + C_2 e^{-\frac{x-t_b}{L_n}} - e^{-\alpha x}\right) \tag{3.1}$$

where

$$C_1 = \frac{(\alpha D_n + s_1)(\frac{D_n}{L_n} - s_2) - (\alpha D_n - s_2)(\frac{D_n}{L_n} + s_1)e^{-[t_b(\alpha - 1/L_n)]}}{2[\frac{D_n}{L_n}(s_1 + s_2)\cosh(\frac{t_b}{L_n}) + (s_1 s_2 + \frac{D_n^2}{L_n^2})\sinh(\frac{t_b}{L_n})]} \tag{3.2}$$

$$C_2 = \frac{(\alpha D_n + s_1)(\frac{D_n}{L_n} + s_2) - (\alpha D_n - s_2)(\frac{D_n}{L_n} - s_1)e^{-[t_b(\alpha + 1/L_n)]}}{2[\frac{D_n}{L_n}(s_1 + s_2)\cosh(\frac{t_b}{L_n}) + (s_1 s_2 + \frac{D_n^2}{L_n^2})\sinh(\frac{t_b}{L_n})]} \tag{3.3}$$

$\theta_3$ is the reflection angle of the incident pump beam in the CIGS layer, $\alpha$, $\phi_0$, R, and T are the absorption coefficient, photon flux, total front surface reflectance, and back-interface transmittance at a given pump beam wavelength, while $D_n$, $t_b$, $\tau$, $s_1$, and $s_2$ are the diffusion coefficient, CIGS film thickness, excess carrier lifetime, front-surface recombination velocity and back-interface recombination velocity in the CIGS films, respectively.

When pump beam is off, the reflected intensity of the probe beam I can be expressed in terms of the transmitted intensity $I_0$, electron density $n_0$, hole density $p_0$, and the optical absorption cross section of electrons and holes, $\sigma_n$ and $\sigma_p$, respectively, as

$$I = I_0 R' \exp[-2\int_0^{t_b}(\sigma_n n_0 + \sigma_p p_0)dx] \tag{3.4}$$

When pump beam is turned on, the excess carriers generated in the CIGS film will modulate the IR reflected beam intensity. Under low injection conditions, the reflected intensity of the probe beam $I'$ can be express as

$$I' = I_0 R' \exp[-2\Delta N \sigma_{fc} - 2\int_0^{t_b} (\sigma_n n_0 + \sigma_p p_0) dx] \qquad (3.5)$$

where

$$\Delta N = \int_0^{t_b} \Delta n(x) dx \qquad (3.6)$$

$$= \frac{\alpha \phi_0 (1 - R - T)\cos\theta_3}{D_n(\alpha^2 - \frac{1}{L_n^2})} [L_n C_1 (1 - e^{-\frac{t_b}{L_n}}) - L_n C_2 (1 - e^{\frac{t_b}{L_n}}) + \frac{1}{\alpha}(e^{-\alpha t_b} - 1)]$$

R' is the reflectance at Mo/CIGS interface, $\sigma_{fc} = \sigma_n + \sigma_p$ is the total optical absorption cross-section of electrons and holes.

For ΔI<<I, the fractional change in the probe beam intensity ΔI/I (with ΔI = I' – I) can be expressed as

$$\ln(\frac{\Delta I}{I} + 1) \cong \frac{\Delta I}{I} = -2\sigma_{fc} \Delta N \qquad (3.7)$$

$$= -2\sigma_{fc} \{\frac{\alpha \phi_0 (1 - R - T)\cos\theta_3}{D_n(\alpha^2 - \frac{1}{L_n^2})} [L_n C_1 (1 - e^{-\frac{t_b}{L_n}}) - L_n C_2 (1 - e^{\frac{t_b}{L_n}}) + \frac{1}{\alpha}(e^{-\alpha t_b} - 1)]\}$$

Since the absorption coefficient ($\alpha \approx 8\times10^4$ cm$^{-1}$) is very high in the CIGS film for the wavelength of the pump beam (He-Ne laser, λ=632.8nm), and the bulk trap density in the CIGS film is high [63, 66], the following assumptions prevail for DBOM analysis: (i) $\alpha L_n >> 1$, (ii) $\alpha D_n >> s_1, s_2$, (iii) $D_n^2 >> s_1 s_2 L_n^2$. Based on these assumptions and solving equations (3.1) through (3.7), the fractional change in the probe-beam reflected intensity $\Delta I/I$ can be expressed as

$$\frac{\Delta I}{I} = -2\sigma_{fc}\cos\theta_3\phi_0(1-R-T)\tau_{eff}(1-e^{-\alpha t_b}) \tag{3.8}$$

where

$$\tau_{eff} = \frac{t_b}{s_1 + t_b/\tau} \tag{3.9}$$

is the effective excess carrier lifetime in the CIGS film, which reduces to the bulk film lifetime if the front surface recombination velocity $s_1$ is much smaller than $t_b/\tau$. Thus, the excess carrier lifetimes in a CIGS film can be obtained by using the values of $\Delta I$ and I obtained from the DBOM measurements, and the calculated values of R and T.

The total transmittance and reflectance can be expressed as (* denotes the complex conjugate)

$$T = t \times t^* \tag{3.10}$$

$$R = r \times r^* \tag{3.11}$$

The total transmission and reflection coefficients can be expressed as [67, 68]

$$t = \frac{t_0 t_1 t_2 e^{-i(\delta_1+\delta_2)/2}}{1 + r_0 r_1 e^{-i\delta_1} + r_1 r_2 e^{-i\delta_2} + r_0 r_2 e^{-i(\delta_1+\delta_2)/2}} \tag{3.12}$$

and

$$r = \frac{r_0 + r_1 e^{-i\delta_1} + r_2 e^{-i(\delta_1+\delta_2)} + r_0 r_1 r_2 e^{-i\delta_2}}{1 + r_0 r_1 e^{-i\delta_1} + r_1 r_2 e^{-i\delta_2} + r_0 r_2 e^{-i(\delta_1+\delta_2)}} \tag{3.13}$$

where

$$\delta_1 = \frac{4\pi}{\lambda} n_{CdS} t_{CdS} \cos\theta_2 \tag{3.14}$$

$$\delta_2 = \frac{4\pi}{\lambda} n_{CIGS} t_b \cos\theta_3 \tag{3.15}$$

where $t_0$, $t_1$, and $t_2$ are the Fresnel transmission coefficients at the air/Cds film, CdS film/CIGS film, and CIGS film/Mo film interfaces, respectively; $r_0$, $r_1$, and $r_2$ are the Fresnel transmission coefficients at the air/Cds film, CdS film/CIGS film, and CIGS film/Mo film interfaces, respectively; $\delta_1$ and $\delta_2$ are the phase changes that result from the double travel of light in the CdS layer and CIGS films; $\lambda$ is the wavelength of the incident light (laser pump beam); $t_{CdS}$, $t_b$, $\theta_2$, and $\theta_3$ are the thickness of CdS layer, thickness of CIGS film, and refraction angles in the CdS layer and CIGS film, respectively; $n_{CdS}$ is the refraction index of the CdS layer; $n_{CIGS}$ is the refractive index of the CIGS film and $n_{CIGS} = N_{CIGS} + ik$, where $N_{CIGS}$ and k (= $\alpha\lambda/4\pi$) are the real and imaginary parts of the refractive index [69]; and $\alpha$ is the optical absorption coefficient of CIGS film. The Fresnel transmission and reflection coefficients are given by

$$t_0 = \frac{2\cos\theta_1}{\cos\theta_1 + n_{CdS}\cos\theta_2} \tag{3.16}$$

$$t_1 = \frac{2n_{CdS}\cos\theta_2}{n_{CdS}\cos\theta_2 + n_{CIGS}\cos\theta_3} \tag{3.17}$$

$$t_2 = \frac{2n_{CIGS}\cos\theta_3}{n_{CIGS}\cos\theta_3 + n_{Mo}\cos\theta_4} \tag{3.18}$$

$$r_0 = \frac{\cos\theta_1 - n_{CdS}\cos\theta_2}{\cos\theta_1 + n_{CdS}\cos\theta_2} \tag{3.19}$$

$$r_1 = \frac{n_{CdS}\cos\theta_2 - n_{CIGS}\cos\theta_3}{n_{CdS}\cos\theta_2 + n_{CIGS}\cos\theta_3} \tag{3.20}$$

$$r_2 = \frac{n_{CIGS}\cos\theta_3 - n_{Mo}\cos\theta_4}{n_{CIGS}\cos\theta_3 + n_{Mo}\cos\theta_4} \qquad (3.21)$$

where $n_{Mo}$ is the refraction index of the Mo layer, $\theta_4$ is refraction angle in the Mo layer.

Thus the total transmittance T and reflectance R can be obtained by substituting equations (3.12) through (3.21) into equations (3.10) and (3.11). In addition, by measuring the total reflectance, the thickness of CdS layer and CIGS film can be determined by using a contactless dual beam S-polarized reflectance (DBSPR) technique [70], which was originally developed to determine the silicon film and buried oxide thickness in SOI materials. Once the total transmittance T and reflectance R are obtained from equations (3.10) and (3.11), the excess carrier lifetimes can be carried out by substituting T and R into equation (3.8).

## Experimental Details

### Lifetime Measurement

As shown in Fig. 3-2, a long-pass filter with a cutoff wavelength $\lambda_c = 1350$ *nm* ,which is placed between test samples and detector, is used to block the undesired signal, namely the photoluminescence (PL) of CIGS material. A tungsten lamp and a He-Ne CW laser ($\lambda = 632.8$nm) are used as probe beam and pump beam, respectively.

The experimental procedure is composed of two steps. First, the reflected intensity I of an IR probe beam (with $h\nu < E_g$ of CIGS) is measured by chopping the tungsten lamp, and the signal is detected with a lock-in amplifier. Second, the change in the reflected beam intensity ΔI, due to a modulated pump beam ($h\nu \geq E_g$), is measured by using the chopped pump beam, and the resulting IR reflected beam intensity is measured using a lock-in amplifier.

**Buffer Layer Processing**

Three different CdS processing methods (CBD, MOCVD, and sputtering) were used for the deposition of CdS buffer layers on the Mo-coated CIGS samples, which were supplied by National Renewal Energy Laboratory (NREL), Siemens Solar Industries (SSI), and Energy Photovoltaics Inc. (EPV). Prior to buffer layer processing, intermediate surface treatments (i.e., as deposited, DI water rinsed, Cd- and S-partial electrolyte treatment, and Ar plasma cleaned) were also applied to some of these samples. The DBOM measurements were performed on samples with or without the CdS buffer layers deposited by these processing techniques.

Two sets of CIGS films were grown on soda-lime glass substrates coated with thick Mo films at NREL. For set-one samples, EPMA data taken on these substrates showed Cu 23.72% (± 0.123%), In 18.76 (± 0.11%), Ga 7.2% (± 0.06%), and Se 50.3% (± 0.09%). All of these substrates were further divided, and ESCA measurements of the surface and near-surface composition profiles were taken. The ESCA data showed that surfaces of all these films were significantly enriched with indium with respect to their average compositions and the composition in the copper-depleted near-surface region. Figure 3-3 schematically illustrates four processing conditions studied and measurements conducted in each case. The baseline CBD solution consisted of $NH_3$ ($1.44\times10^{-4}$M), $NH_4Cl$ ($7.43\times10^{-4}$M), $CdCl_2$ ($2.4\times10^{-4}$M), and $NH_2CSNH_2$ ($2.4\times10^{-3}$M). The cadmium partial electrolyte consisted of a solution with all the same reactant except thiourea, and the sulfur partial electrolyte contained all the baseline reactants in the same concentration except the cadmium salt. The aqueous processing was conducted at a bath temperature of 80-85°C and was continuously stirred. The processing time for the partial electrolyte cases is identical to the baseline CBD process, which produced a uniform, compact, coherent, and colloid-free film with a thickness of about 800Å. MOCVD was performed in a horizontal atmospheric pressure cold wall reactor using dimethyl cadmium and hydrogen sulfide reactants in hydrogen at a substrate temperature of $160\pm10^{\circ}$C and a VI/II reactant ratio of 100/1 for 2.8 minutes. The MOCVD growths were prenucleated with approximately one minute of exposure to $H_2S$ before the flow of dimethyl cadmium began. The DBOM measurements were conducted on sixteen distinct locations for each substrate at each step in the process per Fig. 3-3.

For set-two NREL CIGS samples, the CdS buffer layer was deposited by using the CBD (NREL), sputtering (MRG), and MOCVD (University of Florida) techniques. The processing conditions studied and measurements conducted for these samples are shown in Figure 3-4. These samples measured by DBOM technique were not fabricated into devices but are believed to be comparable to the similar samples with efficiencies of around 14%.

In addition to the samples fabricated by NREL, CIGS films were provided from two different sources (SSI and EPV). The CdS buffer layers for these samples were deposited by using either the CBD (University of Florida) or sputtering (MRG) technique. The CdS deposition (CBD and sputtering) was carried out on the as-deposited CIGS samples and on CIGS samples treated with DI water rinsing and Ar plasma cleaning. These samples measured by DBOM technique were not fabricated into solar cell but are believed to be comparable to similar samples with efficiencies of around 3-5% (best one 9%) fabricated by NREL.

## Results and Discussion

The following results are obtained by using the simplified model (no p-n junction) and the data of ΔI and I measured by the reflection-mode DBOM technique.

### Measurements of NREL Samples

The different processing conditions and measurements conducted in each case are illustrated in the Fig. 3-3 for the first set of NREL samples. Fig. 3-5 is a box plot showing a statistically summary of the excess carrier lifetime data taken for each experiment case, initially (as-received), after intermediate surface treatments (Cd- and S-partial electrolyte), and after the completion of processing. Several results are evident. First, the initial lifetimes in the CIGS films, in the range of smaller than 3ns, are typically improved by a factor of two to three in every case except the aqueous sulfur electrolyte exposure. This result is strong negative evidence for attributing the beneficial effects on CIGS device performance of the CBD CdS process to sulfur passivation, an effect well established in the case of III-V compound semiconductors. However, the data does not support the alternative hypothesis that cadmium ion reactions with the surface during the CBD process alone are responsible for the dramatic lifetime improvement shown in the cadmium partial electrolyte case subsequent to the MOCVD growth of CdS, because the lifetimes measured immediately after aqueous processing showed no significant change compared to their initial values. Indeed, considering the substantially poorer initial lifetime in the MOCVD control sample compared to the CBD control and cadmium partial electrolyte samples, it appears that the beneficial effect is provided equally well by the MOCVD growth process alone. Since all the samples were baked in air before final measurement except the MOCVD control sample, the possibility that oxidation or higher temperature interdiffusion effects are required to achieve high lifetimes is not supported by this data. Since the MOCVD control (which was not subjected to any aqueous processing) had a beneficial effect on lifetimes, and the aqueous sulfur electrolyte exposure a neutral effect, water exposure alone cannot be responsible for the observed lifetime increases.

Figures 3-6, 3-7, 3-8, and 3-9 are the contour-line plots of DBOM data showing the spatial inhomogeneity in excess carrier lifetimes exhibited in these very high quality films initially, after surface treatments, and even for the CIGS samples after the CBD and MOCVD processings. Future studies will use this capability in conjunction with the materials characterization to obtain a correlation with the material parameters and defect structures, which control the recombination processes in these device structures.

It is known that CIGS is the material with photoluminescence (PL). The photoluminescence is the undesired signal for the DBOM measurements. After both the deposition of CdS and annealing process on the sample D, the signal ΔI of DBOM measurement can not be measured correctly. Generally the signal ΔI detected by a lock-in amplifier is in the range of microvolts ($\mu V$). Thus, it is possible that the photoluminescence emission from the CIGS sample affects the DBOM measurement. It is shown that the higher temperature of annealing process on CIGS samples results in the higher PL intensity emission from CIGS samples [71]. This is the reason why the DBOM measurement can not be performed correctly on the sample D after annealing process. According to the PL spectra of CIGS samples [71 and 72], the peak positions of PL intensity are around at wavelength $\lambda = 1280$ *nm*. Therefore a long-pass filter with a cutoff wavelength $\lambda_c = 1350$ *nm* is used to block the undesired signal, photoluminescence emission from CIGS material, and it is set between test samples and detector as shown in Fig. 3-2. With the long-pass filter, the reflection mode DBOM measurement can be performed on CIGS samples without a hitch.

The results for the second set of NREL CIGS samples were determined by the DBOM technique, and are summarized in Tables 3-1, 3-2, and 3-3, Figures 3-10, 3-11, and 3-12. Table 3-1 and Fig. 3-10 show a statistical summary of the excess carrier lifetimes taken for the experimental cases of as deposited, after DI water rinsed, after Cd partial electrolyte, and after annealing at 200°C for 2 minutes for the samples without CdS. Table 3-2 and Fig. 3-11 summarize the excess carrier lifetimes of the samples without CdS and with CBD, MOCVD, and sputtering deposited CdS and with different surface treatments. For discussing the MOCVD CdS process, Table 3-3 and Fig. 3-12 show the excess carrier lifetimes for each experimental condition: as deposited, after surface treatments, and after MOCVD CdS. And the contour-line plots of excess carrier lifetimes for three CIGS samples as deposited initially, after surface treatments, and MOCVD CdS deposition are shown in Figures 3-13, 3-14, and 3-15. It should be pointed out that there is a considerable variation in the excess carrier lifetimes for the as-deposited CIGS samples without CdS, as is shown in Table 3-1 and Fig. 3-10, respectively. One of the difficulties in interpreting the DBOM results in these CIGS samples is the fact that we have only the samples with the CBD as well as sputtering CdS deposition and we do not have the DBOM measurements (and hence the excess carrier lifetimes) on these CIGS samples prior the deposition of CdS.

The effect of CdS deposition on the excess carrier lifetimes in CIGS films is obvious. The results reveal that the excess carrier lifetimes are significantly increased with CdS deposition. The CIGS samples with the sputtered CdS show a dramatic increase in excess carrier lifetimes for both the as-deposited and after surface treatments. However, no clear evidence of positive effect of the surface treatments (DI water rinsing and Cd partial electrolyte treatments) and annealing on the excess carrier lifetimes in these CIGS samples is obtained from this study. It is interesting to note that the most dramatic increase in the excess carrier lifetimes was observed in the sputtered CdS deposited samples with no intermediate surface treatments. Also, the direct processing of sputtered CdS on the as-grown CIGS sample yields the longest excess carrier lifetime when compared to the CdS deposited CIGS samples.

### Measurements of SSI and EPV Samples

The DBOM results for these samples are shown in Fig. 3-16. No detectable DBOM signal was obtained on all CIGS samples without the CdS buffer layers, as shown in Fig. 3-16. It is obvious that the CdS buffer layers increase $\Delta I/I$ values (and hence excess carrier lifetimes) for both the DI water-treated and as-deposited samples. This is especially true for the sputtering CdS deposited CIGS samples which show a dramatic increase of the DBOM signal for those DI water-treated and as deposited samples, as illustrated in Fig. 3-16. For both the CBD and sputtering CdS deposited samples, the DI water rinsing treatment decreases the excess carrier lifetimes. It is interesting to point out that the Ar plasma cleaning process dramatically increases the DBOM signal for the samples without the CdS buffer layer. The Ar plasma cleaning has the effects of Ar ion bombardment on the surface of the CIGS samples. Thus a smaller depletion width could have been created in the surface junction because of the Ar-plasma cleaning process. After Ar-plasma cleaning process, according to the XPS analysis the data show a clear evidence of chemical change in the samples, especially near the surface. The Cu/In ratio is restored to around unity although the starting surface composition was heavily In-rich. The depletion width created due to the chemical change near the surface of the CIGS film could be the reason why the similar samples fabricated into devices have an increase in $V_{oc}$ compared to the cells fabricated by using the as-grown and DI water rinsed samples. The created small depletion width and the band bending do have an effect on the results of DBOM measurements, which show an increase in the DBOM signal. However, after the sputtering CdS process on the CIGS samples the DBOM signal decreases.

## Conclusions

We have demonstrated a contactless reflection mode DBOM technique developed specifically for determining the excess carrier lifetimes in the CIS and CIGS films. A study of the effects of CBD, MOCVD and sputtering deposited CdS on the excess carrier lifetimes in the CIGS films has been conducted. The results of this DBOM study for the CIGS samples from different laboratories (NREL, EPV, and SSI) are summarized as follows: the CBD, MOCVD and sputtering deposited CdS buffer-layer formation increase the excess carrier lifetimes for all as-deposited, water-rinsed, S- and Cd-partial electrolyte-treated samples. The CdS deposition increases ΔI/I less for water-rinsed, S- and Cd-partial electrolyte-treated samples than for as-deposited samples. Sputtering CdS deposition decreases the excess carrier lifetimes for the Ar-plasma cleaned samples. However, prior to the CdS deposition, Ar-plasma cleaning process exclusively increases the excess carrier lifetimes of CIGS films. The intermediate surface treatments (i.e., DI water rinsed, Cd-partial electrolyte treatment, and Ar plasma cleaned) are not a positive effect on excess carrier lifetimes for CdS deposited CIGS samples. Especially, the sputtering of CdS dramatically increases the DBOM signal ΔI/I for as-deposited, water- and Cd-partial electrolyte-treated samples. The relative free carrier absorption change as measured by ΔI/I shows consistent trends for the CIGS films from several laboratories fabricated by the different techniques. The free carrier absorption change measured by the DBOM signal can be directly related to the quality of CIGS films studied in this work.

Further study of the correlation between the excess carrier lifetimes and the performance parameters of CIGS solar cells will be carried out in order to optimize the processing and growth conditions of CIGS films.

Table 3-1. The excess carrier lifetimes $\tau_{eff}$ (ns) of the CIGS samples without CdS

| sample # | As deposited | DI water rinsed | Cd partial electrolyte | Annealing |
|---|---|---|---|---|
| M1517-A | 1.46 | --- | 1.34 | 1.43 |
| M1517-B | 1.90 | 1.73 | --- | 1.75 |
| M1517-C | 0.77 | --- | --- | --- |

Table 3-2. The average excess carrier lifetimes of NREL samples

| | As deposited | | DI water rinsed | | Cd partial electrolyte | |
|---|---|---|---|---|---|---|
| | sample # | $\tau_{eff}$ (ns) | sample # | $\tau_{eff}$ (ns) | sample # | $\tau_{eff}$ (ns) |
| no CdS | M1517C | 0.77 | M1517B | 1.75 | M1517A | 1.43 |
| CBD CdS | M1518C | 3.95 | M1518B | 2.76 | M1518A | 3.56 |
| MOCVD CdS | M1518F | 17.6 | M1518E | 1.91 | M1518D | 4.67 |
| Sputtered CdS | M1518I | 12.7 | M1518H | 7.64 | M1518G | 5.48 |

Table 3-3. The excess carrier lifetimes $\tau_{eff}$ (ns) of NREL CIGS samples for MOCVD CdS

| sample # | As deposited | DI water rinsed | Cd partial electrolyte | MOVCD CdS |
|---|---|---|---|---|
| M1518-D | 2.29 | --- | 2.08 | 4.67 |
| M1518-E | 1.71 | 1.70 | --- | 1.91 |
| M1518-F | 0.53 | --- | --- | 17.6 |

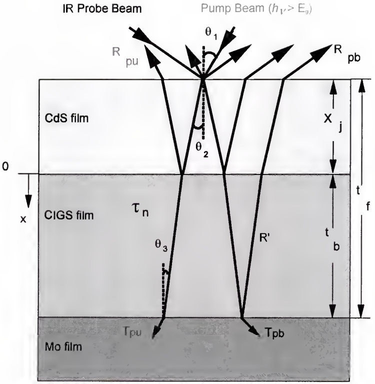

Figure 3-1. Cross sectional view of CIGS cell used in the simplified DBOM theory

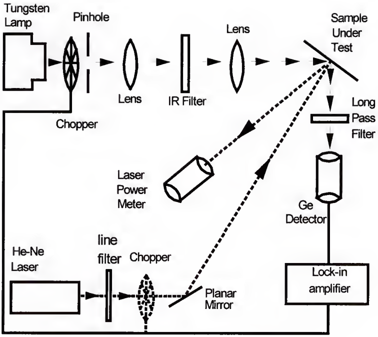

Figure 3-2. Schematic diagram of reflection mode DBOM setup with a long pass filter

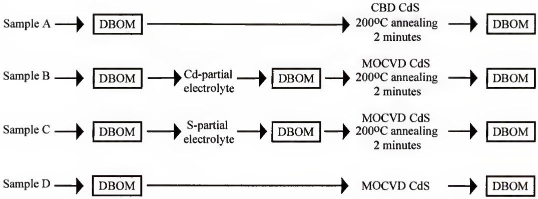

Figure 3-3. Process flow sequence of NREL CIGS samples for the four experimental conditions

Sample number M1517

| | | |
|---|---|---|
| As deposited<br>C | DI water<br>B | Cd electrolyte<br>A |
| | | |
| | | |

Sample number M1518

| | | | |
|---|---|---|---|
| CBD CdS → | As deposited<br>C | DI water<br>B | Cd electrolyte<br>A |
| MOCVD CdS → | As deposited<br>F | DI water<br>E | Cd electrolyte<br>D |
| Sputtering CdS → | As deposited<br>I | DI water<br>H | Cd electrolyte<br>G |

Figure 3-4. The twelve experimental conditions for NREL CIGS samples

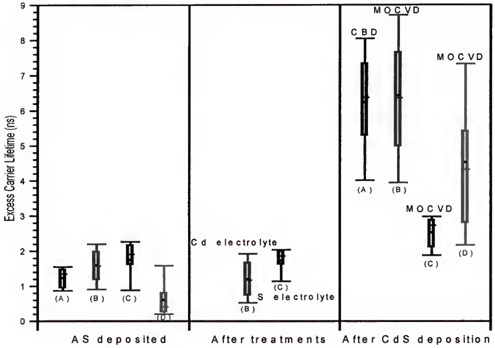

Figure 3-5. A statistical summary of excess carrier lifetimes for the first set NREL CIGS samples

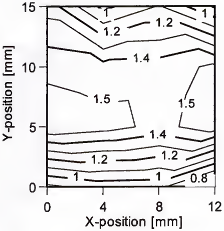

(a) Initially

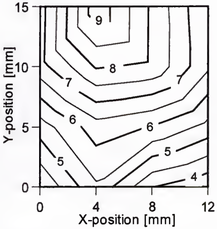

(b) After CBD deposited CdS

Figure 3-6. Contour line plot of excess carrier lifetimes for NREL CIGS sample (a) initially (as deposited) (b) after CBD deposited CdS

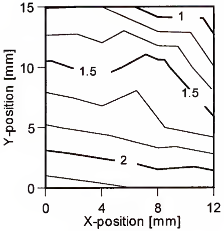

(a) Initially

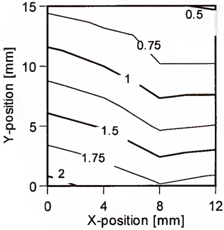

(b) After surface treatment

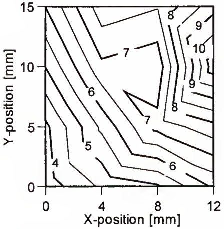

(c) After MOCVD deposited CdS

Figure 3-7. Contour line plots of excess carrier lifetimes for NREL CIGS sample (a) initially (as deposited) (b) after surface treatment (Cd-partial electrolyte) (c) after MOCVD deposited CdS

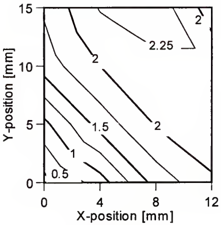

(a) Initially

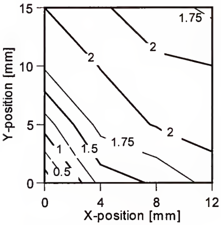

(b) After surface treatment

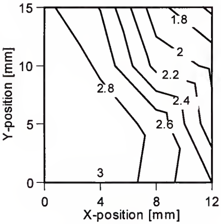

(c) After MOCVD deposited CdS

Figure 3-8. Contour line plots of excess carrier lifetimes for NREL CIGS sample (a) initially (as deposited) (b) after surface treatment (S-partial electrolyte) (c) after MOCVD deposited CdS

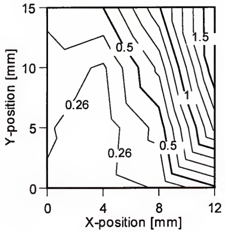

(a) Initially

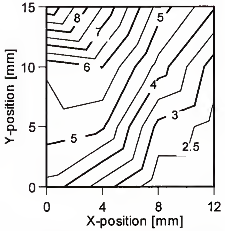

(b) After MOCVD deposited CdS

Figure 3-9. Contour line plot of excess carrier lifetimes for NREL CIGS sample (a) initially (as deposited) (b) after MOCVD deposited CdS

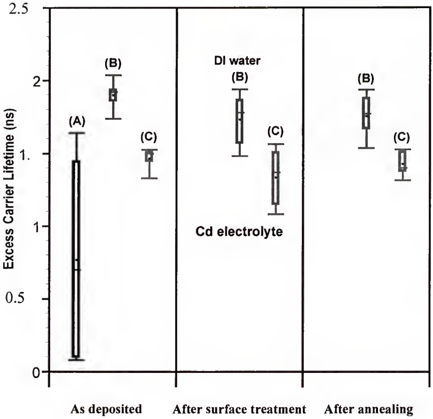

Figure 3-10. A statistical summary of excess carrier lifetimes for the second set NREL CIGS samples (M1517-A,B and C), the experimental conditions: as deposited, after surface treatments and after annealing.

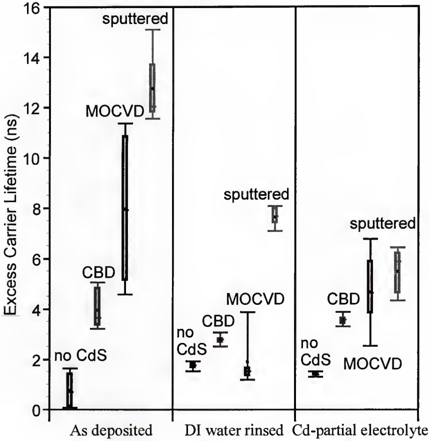

Figure 3-11. A statistical summary of excess carrier lifetime for the second set NREL CIGS samples without CdS and with CBD, MOCVD, and sputtering deposited CdS and with surface treatments.

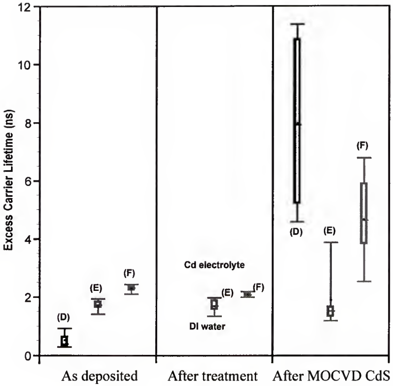

Figure 3-12. A statistical summary of excess carrier lifetimes for MOCVD CdS deposited CIGS samples

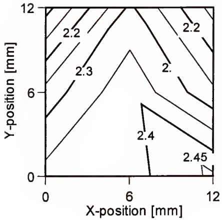

(a) Initially

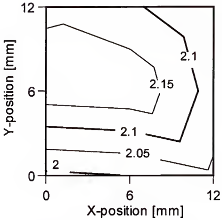

(b) After surface treatment

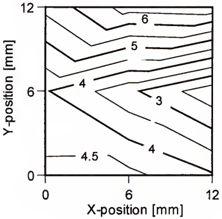

(c) After MOCVD deposited CdS

Figure 3-13. Contour line plots of excess carrier lifetimes for NREL CIGS sample (a) initially (as deposited) (b) after surface treatment (Cd-partial electrolyte) (c) after MOCVD deposited CdS

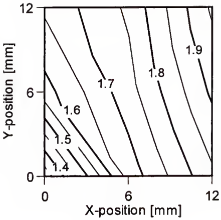

(a) Initially

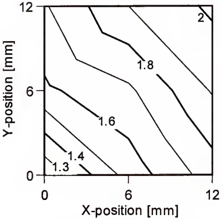

(b) After surface treatment

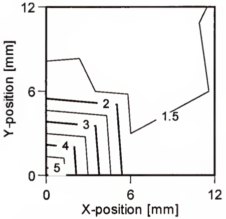

(c) After MOCVD deposited CdS

Figure 3-14. Contour line plots of excess carrier lifetimes for NREL CIGS sample (a) initially (as deposited) (b) after surface treatment (DI water rinsed) (c) after MOCVD deposited CdS

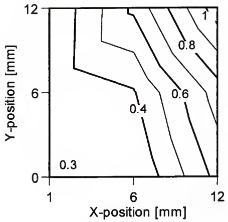

(a) Initially

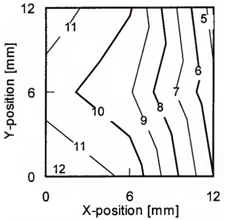

(b) After MOCVD deposited CdS

Figure 3-15. Contour line plot of excess carrier lifetimes for NREL CIGS sample (a) initially (as deposited) (b) after MOCVD deposited CdS

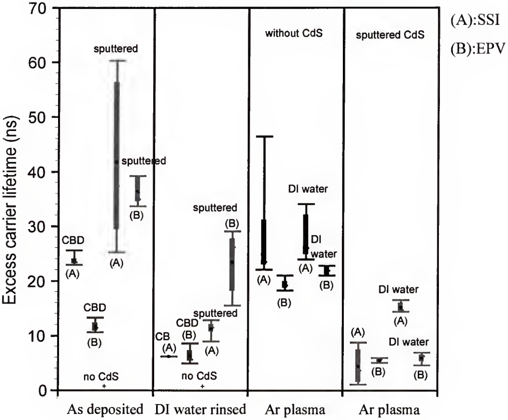

Figure 3-16. A statistical summary of excess carrier lifetimes for SSI and EPV CIGS samples without CdS and with CBD and sputtering deposited CdS, and with surface treatments

# CHAPTER 4

# MODIFIED THEORY FOR REFLECTION MODE DUAL BEAM OPTICAL MODULATION TECHNIQUE

## Introduction

With the deposition of CdS layer on a CIGS film, the CIGS cell is considered as a structure of p-n junction. Thus a depletion layer should be created between the n-type CdS layer and the p-type CIGS film. The formation of CdS buffer layer also results in the energy-band bending in the CIGS cell. As discussed in Chapter 3, the effective excess carrier lifetimes in CIGS films show a significant increase, which is measured by the reflection mode DBOM technique, after the CdS buffer-layer formation on the top of CIGS film. As a matter of fact, this deposition of Cd layer results in an increase in DBOM signal ΔI/I (the change in the reflected beam intensity ΔI over the reflected intensity I of the IR probe beam) which is related to the change of free carrier absorption and of excess carrier lifetimes in the CIGS layer. The increase of DBOM signals may be attributed to the creation of depletion layer and band bending effect. Considering the depletion layer width W of the CIGS cell as zero, the simplified DBOM model used in Chapter 3 should be modified to take this depletion layer into account in order to more accurately interpret the DBOM measurements for the CIS and CIGS films. Thus an modified analytical DBOM model for the CIS and CIGS p-n junction cells is derived which contains the functional change dependence of ΔI/I on the excess carrier lifetimes, diffusion length of minority carriers, depletion layer width, and surface/interface recombination velocities.

## Modified DBOM Model for CIGS P-N Junction Cells

As shown in Figure 4-1, a CW laser impinging upon a CIGS sample with a p-n junction. The excess hole concentration $\Delta p(x)$ in the CdS layer and excess electron concentration $\Delta n(x)$ in the CIGS layer can be obtained by solving the continuity equations

$$D_p \frac{\partial^2 \Delta p(x)}{\partial x^2} - \frac{\Delta p(x)}{\tau_p} + G(x) = 0 \qquad \text{in the CdS layer} \qquad (4.1)$$

and

$$D_n \frac{\partial^2 \Delta n(x)}{\partial x^2} - \frac{\Delta n(x)}{\tau_n} + G(x) = 0 \qquad \text{in the CIGS layer} \qquad (4.2)$$

with boundary conditions given by

$$D_p \left.\frac{\partial \Delta p(x)}{\partial x}\right|_{x=0} = s_1 \Delta p(0) \qquad [x = 0] \qquad (4.3)$$

$$\Delta p(X_j) = 0 \qquad [x = X_j] \qquad (4.4)$$

$$\Delta n(X_j + W) = 0 \qquad [x = X_j + W] \qquad (4.5)$$

$$-D_n \left.\frac{\partial \Delta n(x)}{\partial x}\right|_{x=t_f} = s_2 \Delta n(t_f) \qquad [x = t_f] \qquad (4.6)$$

and the generation rate G(x) can be expressed as

$$G(x) = \alpha_{CdS} \phi_0 \cos\theta_3 (1 - R - T) e^{-\alpha_{CdS} x} \qquad \text{in the CdS layer} \qquad (4.7)$$

$$G(x) = \alpha_{CIGS} \phi_0 \cos\theta_3 (1 - R - T) e^{-\alpha_{CIGS} (x + X_j + W)} \qquad \text{in the CIGS layer} \qquad (4.8)$$

where $\alpha_{CdS}$, $\alpha_{CIGS}$, $\phi_0$, R, and T are the absorption coefficients for CdS and CIGS, photon flux, total front surface reflectance, and back-interface transmittance at a given pump beam wavelength, while $D_n$, $D_p$, $X_j$, W, $t_b$, $\tau_p$, $\tau_n$, $s_1$, and $s_2$ are the diffusion coefficients in the CdS layer and in the p-type CIGS layer, CdS layer thickness, space charge layer thickness, CIGS film thickness, excess carrier lifetimes in the CdS layer and in the p-type CIGS layer, surface recombination velocity in the CdS layer, and back-interface recombination velocity in the CIGS films, respectively.

The excess hole concentration in the CdS layer and excess electron concentration can be obtained by solving equations (4.1) and (4.2) with boundary conditions

$$\Delta p(x) = \frac{\alpha_{CdS}\cos\theta_3\phi_0(1-R-T)}{D_p(\alpha_{CdS}{}^2 - \frac{1}{L_p^2})}\left[\frac{(\alpha_{CdS}L_p + \frac{L_p}{D_p}s_1)\sinh(\frac{X_j - x}{L_p})}{C_1} + \frac{\frac{L_p}{D_p}s_1\sinh(\frac{x}{L_p})e^{-\alpha_{CdS}X_j}}{C_1} + \frac{\cosh(\frac{x}{L_p})e^{-\alpha_{CdS}X_j}}{C_1} - e^{-\alpha_{CdS}x}\right] \tag{4.9}$$

$$\Delta n(x) = \frac{\alpha_{CIGS}\cos\theta_3\phi_0(1-R-T)}{D_n(\alpha_{CIGS}{}^2 - \frac{1}{L_n^2})}e^{-\alpha_{CIGS}(X_j+W)}\left[\cosh(\frac{x - X_j - W}{L_n}) - e^{-\alpha_{CIGS}(x - X_j - W)} - C_2\sinh(\frac{x - X_j - W}{L_n})\right] \tag{4.10}$$

where $$C_1 = \frac{L_p}{D_p}s_1\sinh(\frac{X_j}{L_p}) + \cosh(\frac{X_j}{L_p}) \tag{4.11}$$

$$C_2 = \frac{\frac{L_n}{D_n} s_2[\cosh(\frac{t_b}{L_n}) - e^{-\alpha_{CIGS}t_b}] + \sinh(\frac{t_b}{L_n}) + \alpha_{CIGS} L_n e^{-\alpha_{CIGS}t_b}}{\frac{L_n}{D_n} s_2 \sinh(\frac{t_b}{L_n}) + \cosh(\frac{t_b}{L_n})} \tag{4.12}$$

$\theta_3$ is the reflection angle of the incident pump beam in the CIGS layer, $t_b = t_f - X_j - W$ is the thickness of p-type CIGS layer, $L_p = (D_p\tau_p)^{1/2}$ and $L_n = (D_n\tau_n)^{1/2}$ are the diffusion lengths of the minority carriers in the CdS layer and CIGS layer, respectively. When the pump beam is turned on, the excess carriers generated in the CIGS film will modulate the IR transmitted beam intensity. Without pump beam, the transmitted intensity of the probe beam I can be expressed in terms of the unmodulated transmitted intensity $I_0$, electron density $n_0$, hole density $p_0$ in the absence of pump beam excitation, and the total optical absorption cross section $\sigma_{fc} = \sigma_n + \sigma_p$ as

$$I = I_0 R' \exp\left[-2\int_0^{t_f} (\sigma_n n_0 + \sigma_p p_0) dx\right] \tag{4.13}$$

and under low injection conditions, the transmitted intensity of the probe beam $I'$ can be expressed as

$$I' = I_0 R' \exp\left[-2(\Delta N \sigma_{CIGS} + \Delta P \sigma_{CdS}) - 2\int_0^{t_f} (\sigma_n n_0 + \sigma_p p_0) dx\right] \tag{4.14}$$

where $$\Delta N = \int_{X_j+W}^{t_f} \Delta n(x) dx$$

$$= \int_{X_j+W}^{t_f} \frac{\alpha_{CIGS}\cos\theta_3\phi_0(1-R-T)}{D_n\left(\alpha_{CIGS}^2 - 1/L_n^2\right)} e^{-\alpha_{CIGS}(X_j+W)} \Bigg[\cosh\left(\frac{x-X_j-W}{L_n}\right) - e^{-\alpha_{CIGS}(x-X_j-W)} - C_2\sinh\left(\frac{x-X_j-W}{L_n}\right)\Bigg]dx$$

$$= \tau_n \frac{\alpha_{CIGS}\cos\theta_3\phi_0(1-R-T)}{\alpha_{CIGS}^2 L_n^2 - 1} e^{-\alpha_{CIGS}(X_j+W)} \Bigg\{L_n\sinh\left(\frac{t_f-X_j-W}{L_n}\right) - \frac{1-e^{-\alpha_{CIGS}(t_f-X_j-W)}}{\alpha_{CIGS}} - C_2L_n\left[\cosh\left(\frac{t_f-X_j-W}{L_n}\right)-1\right]\Bigg]\Bigg\} \tag{4.15}$$

$$\Delta P = \int_0^{X_j} \Delta p(x)dx$$

$$= \int_0^{X_j} \frac{\alpha_{CdS}\cos\theta_3\phi_0(1-R-T)}{D_p\left(\alpha_{CdS}^2 - 1/L_p^2\right)} \Bigg[\frac{\alpha_{CdS}L_p + s_1 L_p/D_p}{C_1}\sinh\left(\frac{X_j-x}{L_p}\right) + \frac{e^{-\alpha X_j}s_1 L_p/D_p}{C_1}\sinh\left(\frac{X_j}{L_p}\right) + \frac{e^{-\alpha X_j}}{C_1}\cosh\left(\frac{X_j}{L_p}\right) - e^{-\alpha x}\Bigg]dx$$

$$= \tau_p \frac{\alpha_{CdS}\cos\theta_3\phi_0(1-R-T)}{\alpha_{CdS}^2 L_p^2 - 1} \Bigg\{\frac{L_p}{C_1}\left[\cosh\left(\frac{X_j}{L_p}\right)-1\right]\left(\alpha_{CdS}L_p + \frac{L_p}{D_p}s_1 + \frac{L_p}{D_p}s_1 e^{-\alpha_{CdS}X_j}\right) + \frac{e^{-\alpha_{CdS}X_j}}{C_1}L_p\sinh\left(\frac{X_j}{L_p}\right) + \frac{1}{\alpha_{CdS}}\left(e^{-\alpha_{CdS}X_j}-1\right)\Bigg\} \tag{4.16}$$

R' is the reflectance at CIGS/Mo interface, $\sigma_{CIGS} = \sigma_n + \sigma_p$ is the total optical absorption cross-section of electrons and holes in the CIGS layer and $\sigma_{Cds}$ is the total optical cross-section in the CdS layer.

For $\Delta I \ll I$, the fractional change in the probe beam intensity $\Delta I/I$ (with $\Delta I = I' - I$) can be solved from equations (5.13) and (5.14), and the result yields

$$\ln(\frac{\Delta I}{I}+1) \cong \frac{\Delta I}{I} = -2(\sigma_{CIGS}\Delta N + \sigma_{Cds}\Delta P) \tag{4.17}$$

$$\begin{aligned}\frac{\Delta I}{I} = -2\cos\theta_3\phi_0(1-R-T)\Bigg\langle \tau_n\sigma_{CIGS}\frac{\alpha_{CIGS}e^{-\alpha_{CIGS}(X_j+W)}}{\alpha_{CIGS}^2 L_n{}^2-1}\Bigg\{L_n\sinh\left(\frac{t_f-X_j-W}{L_n}\right)\\ -C_2L_n\left[\cosh\left(\frac{t_f-X_j-W}{L_n}\right)-1\right]-\frac{1}{\alpha_{CIGS}}\left[1-e^{-\alpha_{CIGS}(t_f-X_j-W)}\right]\Bigg\}\\ +\tau_p\sigma_{CdS}\frac{\alpha_{CdS}}{\alpha_{CdS}^2L_p{}^2-1}\Bigg\{\frac{L_p}{C_1}\left[\cosh\left(\frac{X_j}{L_p}\right)-1\right]\left(\alpha_{CdS}L_p+\frac{\tau_pS_1}{L_p}+\frac{\tau_pS_1}{L_p}e^{-\alpha_{CdS}X_j}\right)\\ +\frac{e^{-\alpha_{CdS}X_j}}{C_1}L_p\sinh\left(\frac{X_j}{L_p}\right)+\frac{1}{\alpha_{CdS}}\left(e^{-\alpha_{CdS}X_j}-1\right)\Bigg\}\Bigg\rangle\end{aligned} \tag{4.18}$$

Note that the photon energy *hv* of He-Ne laser ($\lambda_p$ = 632.8nm) is smaller than the bandgap energy $E_g$ of CdS and the absorption coefficient $\alpha_{Cds}$ of CdS drops down to near zero at wavelength $\lambda$ = 632.8nm. Furthermore, the thickness of CdS buffer layer used in the CIGS cell is very thin (around 500 Å) and the surface recombination velocity $s_1$ for CdS layer is large. Thus, the excess carriers $\Delta P$ generated in the CdS layer are much smaller than those $\Delta N$ generated in the CIGS layer. If the excess carrier generated in the CdS layer is negligible, equation (4.18) becomes

$$\frac{\Delta I}{I} = -2\cos\theta_3\phi_0(1-R-T)\tau_n\sigma_{CIGS}\frac{\alpha_{CIGS}e^{-\alpha_{CIGS}(X_j+W)}}{\alpha_{CIGS}^2 L_n{}^2 - 1}\left\{L_n \sinh\left(\frac{t_f - X_j - W}{L_n}\right)\right.$$

$$\left. - C_2 L_n\left[\cosh\left(\frac{t_f - X_j - W}{L_n}\right) - 1\right] - \frac{1}{\alpha_{CIGS}}\left[1 - e^{-\alpha_{CIGS}(t_f - X_j - W)}\right]\right\} \qquad (4.19)$$

Therefore, from equation (4.19) the excess carrier lifetimes $\tau_n$ in the CIGS film can be obtained by using the values of $\Delta I$ and I obtained from the DBOM measurements, the calculated values of R and T, and the values of surface recombination velocity $s_2$, depletion layer width W and diffusion length $L_n$ of CIGS.

## Results and Discussion

A modified DBOM model to account for the effect of depletion layer in the CIGS/CdS p-n junction structure has been developed in order to more accurately interpret the DBOM measurements of the CIGS films.

For the NREL CIGS samples with CBD, MOCVD, and sputtering deposited CdS and with surface treatments, Figure 4-2 shows the average excess carrier lifetimes of CIGS films obtained by using the simplified model and the modified model for the chosen parameters: the surface recombination velocity of CIGS film $s_2 = 4\times10^6$ cm/sec, the depletion width $W = 0.05\ \mu m$, and the diffusion length of minority carrier in CIGS film $L_n$ = 0.6, 0.68, and 0.7 $\mu m$. With equations (4.19) and (4.12), the excess carrier lifetime $\tau_n$ is proportional to the DBOM signal ΔI/I for the modified model, and the simplified model (equation (3.8)) has the same relationship between the effective lifetime $\tau_{eff}$ and DBOM signal ΔI/I. Thus, the lifetimes obtained from the simplified and modified models have the same trend, which is clearly shown in the Fig. 4-2 for the specific parameters. The conclusions of the results obtained from the simplified model discussed in Chapter 3 agree with the results obtained from the modified model.

Figures 4-3, 4-4, and 4-5 show the excess carrier lifetimes versus the diffusion length and depletion width for the NREL CIGS samples with the CBD, MOCVD, and sputtered deposited CdS, respectively. The excess carrier lifetimes of CIGS films will increase when the diffusion length or depletion width increases. The modified model is more sensitive to the change of the diffusion length than that of the depletion width, and it is not sensitive to the change of the surface recombination velocity $s_2$. Once the diffusion length and depletion width of the CIGS film are determined, the excess carrier lifetime of CIGS film can be obtained from this modified model.

## Conclusions

An analytical DBOM model for the CIS and CIGS p-n junction solar cells has been derived. To determine the excess carrier lifetimes in the CIS or CIGS film from this modified model, the knowledge of diffusion length and depletion layer width in the CIS p-n junction device is needed. Although the conclusions and trends of CdS buffer layer processing effects on the excess carrier lifetimes of CIGS films obtained from the simplified DBOM model discussed in Chapter 3 are still valid for the modified DBOM model, the values of excess carrier lifetimes determined from the modified model may not be the same as those obtained from the simplified model.

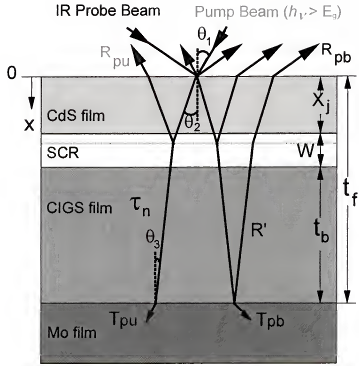

Figure 4-1. Cross sectional view of CIGS p-n junction cell used in the modified DBOM theory

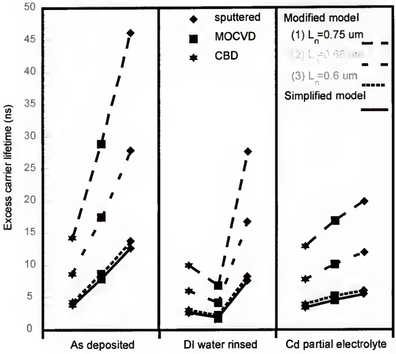

Figure 4-2. A comparison of the average excess carrier lifetimes obtained from the simplified and modified DBOM models for the second set NREL CIGS samples with CBD, MOCVD, and sputtering deposited CdS and with surface treatments. (surface recombination velocity $s_2 = 4\times10^6$ cm/sec, depletion layer width W= 0.05 $\mu m$)

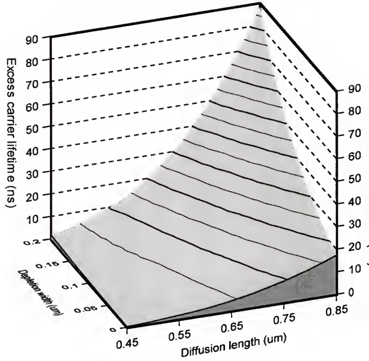

Figure 4-3. Excess carrier lifetimes of CIGS film versus diffusion length and depletion width for NREL CIGS samples with CBD deposited CdS, determined by modified DBOM theory

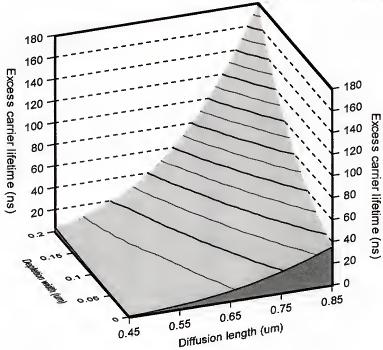

Figure 4-4. Excess carrier lifetimes of CIGS film versus diffusion length and depletion width for NREL CIGS samples with MOCVD deposited CdS, determined by modified DBOM theory

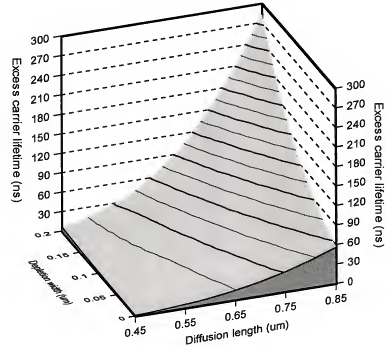

Figure 4-5. Excess carrier lifetimes of CIGS film versus diffusion length and depletion width for NREL CIGS samples with sputtering deposited CdS, determined by modified DBOM theory

# CHAPTER 5
# FABRICATION OF CIS-BASED SOLAR CELLS

## Introduction

A photolithographic process and a simple sequential process are established for the fabrication of the CIS-based solar cells. For the photolithographic process, three photomasks have been specifically designed for patterning the Mo, CIS, and ZnO layers. On the other hand, the sequential fabrication process is applied to make the laboratory-scale CIS solar cells.

## Photolithographic Process

The lithographic process was employed to fabricate CIGS-based solar cells on the 2"x2" Mo-coated soda-lime glass substrates. Three photo-masks for patterning the Mo, CI(G)S, and ZnO layers were designed. Both the positive photoresist for patterning the Mo and ZnO layers and the negative photoresist for patterning the CIS or CIGS layers were applied in the lithographic process. Consequently, a total number of 32 1cm×0.42cm cells were fabricated on a 2"x2" glass substrate. The cells on a single substrate commonly share the top contact and each cell has its individual bottom contact. The detailed process is described below.

The bottom contact Mo layers were first patterned by the photolithographic process in the clean room after the deposition of Mo on the glass substrates. In order to remove the possible contamination introduced during the lithographic process, a cleaning routine including the ultrasonic agitation in the solution of isopropyl alcohol, the vapor drying processing, and the ultraviolet-ozone surface cleaning method was used to clean the surface of Mo substrates after the Mo substrates were patterned.

Subsequently, the CIS films were grown on these patterned Mo substrates. In order to pattern the CIS layers, the solution of methanol with 0.5-3% bromine was used as the etching solution to etch the CIS films. Due to the dissolution of the positive photoresist in methanol, the negative photoresist instead of the positive photoresist was applied. Both dry and wet strippings were employed for the removal of negative resist after patterning the CIS layers. For the dry stripping, the ultraviolet (UV)/ozone cleaning procedure [73] was used to remove the photoresist avoiding the passivation effect. On the other hand, the factory-made chemical "Microstrip" was used to remove the resist for the wet stripping. The deposition of CdS buffer layers can be made before or after the lithographic process for the CIS films. However, the growing of CdS film prior to the lithographic process could provide a protection for the junction between the CdS and CIS layers.

Afterwards, the top contact, a bi-layer of intrisic ZnO and Al-doped ZnO layers, was deposited on the patterned samples by sputtering process in the Department of Material Science and Engineering. Finally, the fabrication of CIS solar cells was completed after the patterning of top contacts was finished.

### Fabrication of Laboratory-Scaled CIS-Based Solar Cells

Typically the size of the CIS-based solar cells fabricated as the test devices in laboratories for the research purposes is very small (around 0.1-1cm$^2$). With the disadvantages of the possible contamination and passivation introduced during the photolithographic process and of time-consuming for the photolithographic process, a simple and easy process was alternatively applied to fabricate the CIS-based solar cells.

Without interruption, the Mo, CIS, buffer, and ZnO layers of CIS solar cells are consecutively deposited by the sputtering, MBE, chemical bath deposition, and sputtering process, respectively. Thus, the contamination can be minimized. The metal grids of Ni and Al layers are then deposited by an e-beam machine. Finally, the cells are completed with the mesa isolation by the mechanical scribing. Each cell on one single substrate shares the same bottom contact but has individual top contact.

# CHAPTER 6
# CURRENT-VERSUS-VOLTAGE AND SPECTRAL RESPONSE MEASUREMENT SYSTEMS

## Introduction

Analysis of current-voltage (I-V) characteristics is one of the most crucial diagnostic tools used to characterize solar cells. The electrical parameters including the conversion efficiency $\eta$, open-circuit voltage $V_{OC}$, short-circuit current density $J_{SC}$, fill factor F.F., series resistance $R_S$, shunt resistance $R_{SH}$, diode ideality factor n, and saturation current density $J_0$ of a solar cell can be determined from the measured dark- and photo-I-V curves. These parameters are important for understanding and optimization of the solar-cell performance. A comparison of the electrical performance of solar cells is meaningful only when the photo-I-V measurements are performed with a certain uniform standard, namely the Standard Reporting Conditions (SRC) specifying the total radiation level, device temperature, and reference spectral radiance distribution. The typical SRC for terrestrial solar cells include a total irradiance of 100 mW/cm$^2$, a reference spectrum of AM1.5 Global (ASTM Standard E892), and a cell junction temperature of 25°C. The I-V measurement system for the characterization of the CIS-based solar cells under SCR was implemented. The apparatus used for the construction of the I-V measurement system and measurement procedure are based on the standard test method for the electrical performance of photovoltaic cells using the reference cells under the simulated sunlight. The measurement apparatus consists of a halogen lamp as the solar simulator, a temperature-controlled test chuck, a programmable power supply as the variable load, the electronic instruments for measuring the terminal voltage and current of the test cells, and a computer program for the control of the measurement procedure and for the data acquisition. The I-V curve of the test cell is measured from the forward bias to the reverse bias using the voltage mode with a resolution of 1mV.

The measurements of the spectral response in terms of the wavelength dependence of the photo-generated current for a solar cell as the characterization and diagnostic techniques are extremely important for the quality control in cell fabrication and cell design. Moreover, the measurement results can provide an understanding in the diffusion mechanisms and separation of the individual photocurrent loss mechanisms. The external quantum efficiency (QE), which is defined as the ratio of the generated electron-hole pairs per incident photon, of the solar cell can be calculated from the measured absolute spectral response curve. A computer-controlled spectral response measurement system using a monochromator for the wavelength selection to measure the spectral response and quantum efficiency (QE) of the CIS-based solar cells was designed and constructed. The measurement system scanning the spectral range from 400 nm to 1400 nm with 10 nm as an increment step has the capability of applying white light bias and voltage bias to the test cell. During the measurement, the entire area of the test cell is covered with a uniform and sufficient illumination-level monochromatic light. A computer program based on the software of *LabVIEW* was used to control the measurement procedure and data acquisition.

# Current-Voltage Measurement Instrumentation and Procedures

## Current-Voltage Measurement Instrumentation

### Solar simulator and irradiance control

The reference cell method, which basically uses the reference cell to adjust the illumination level of the solar simulator, is employed in the performance measurement of CIS and CIGS solar cells. The solar simulator intensity is adjusted by changing the distance between the solar simulator and the test plane so that the measured short-circuit current of the reference cell is equal to its calibrated value at the standard measurement intensity of 100 mW/cm$^2$. The ELH (tungsten-halogen bulb) lamp with an integral dichroic rear reflector is used as the solar simulator in the experimental setup. The ELH lamp is classified as a class C solar simulator by using the ASTM standard procedure E927 due to a lack of energy below the wavelength of 0.5 μm and excess energy in the wavelength range of 0.6-0.7 μm when compared to the global reference spectrum AM1.5G. Using the reference cell method for the efficiency measurements there are always the spectral mismatch errors introduced by the solar simulator and the reference cell due to the difference of the spectrum between the solar simulator and the real solar irradiance at sea level as well as the difference of the spectral response between the reference cell and the test cell. Although we do not intend to directly correct the measured I-V data with the spectral mismatch correction parameter M [74], using a CIGS solar cell calibrated against a primary reference cell and the global reference spectrum by NREL to set the illumination level of the solar simulator can be served as a first order correction for the spectral mismatch in the photo-I-V measurement system.

### Measurement platform and temperature control

The open-circuit voltage of the CIS or CIGS solar cells decreases with increasing temperature at an irradiance power density of 100 mW/cm$^2$ from the solar simulator. In order to have the measurement under the standard reporting conditions (SRC) with both the temperature at 25°C for the cell junction and the illumination intensity of the solar simulator at 100mW/cm$^2$, a thermoelectric cooler assembly with a temperature controller is employed to maintain the temperature of the test cell at 25±1°C during the photo-I-V measurement. Because the CIS and CIGS solar cells are deposited on the glass substrates, a temperature gradient of 3-5°C exists between the top and bottom surfaces of the solar cell when it is under the illumination of the solar simulator. Therefore, the temperature controller of the cooling system is set at about 20°C and a thermocouple is used to monitor the top surface temperature of the test cell to keep the cell temperature at 25±1°C during the measurement. .

### Current-versus-voltage measurements

The four-terminal contacts (also known as the Kelvin connections) are used for the connection between the test cell and the measurement system. Not only the wiring resistance but also the contact resistance between the probe tips and the contact pads of the solar cell can be neglected for the efficiency measurements by using the four-terminal contact method. In addition, a more accurate efficiency measurement for the solar cells can be achieved by using this method. Four micromanipulators with tungsten probe tips whose radii are in the range of 0.6 to 25 μm are used to adjust the position of the probe tips for contacting the small contact pads of the test cell. The voltage and current probes for both the top and bottom contacts should be placed as close as possible to avoid a high voltage drop between the two probes, and the resistance between the voltage and current probes is hence minimized (less than 5Ω).

As illustrated in Figure 6-1, the semi-automated I-V measurement system, which is controlled by a personal computer with the data acquisition and data analysis software *LabVIEW*, is composed of a programmable bipolar power supply served as the variable load, an electrometer for measuring the terminal current, and a digital multimeter for measuring the terminal voltage of the test cell. The measuring range for the current measurements by the electrometer is from 1fA to 20mA. Although the upper limit of the electrometer is only 20mA, the photo-generated current of the CIS cell under test is typically smaller than 20mA due to the small area (nominally 0.429cm$^2$) of the CIS cells fabricated in a laboratory scale. With the sensitivity in the low-current measurements the electrometer with a current resolution of 0.1fA is particularly ideal for the dark-I-V measurement.

### Data acquisition and analysis

A computer program is written in the *LabVIEW* for data acquisition from the readings of the electrometer, multimeter, and power supply. The program also controls the measurement procedure by sending commends to the programmable power supply via the interface of GPIB for the completion of a full sweep of the I-V curve.

### Current-Voltage Measurement Procedures

For the photo-I-V measurements, the illumination intensity of the solar simulator is first set by using the reference cell method depicted above. The test cell is exposed under this condition and biased at around the maximum power point for about 10 minutes (i.e., light soaking effect). The I-V curve is then swept from the forward bias to the reverse bias using the voltage mode with a resolution of 1mV. Using the *LabVIEW* data acquisition software (see Figure 6-2) the basic parameters such as $V_{OC}$, $J_{SC}$, fill factor F.F., output voltage at maximum power point $V_{MAX}$, output current density at maximum power point $J_{MAX}$, maximum power point $P_{MAX}$, and conversion efficiency $\eta$ of test cells can be directly obtained from the measured photo-I-V curves. The open-circuit voltage $V_{OC}$ is determined from a linear fit to the I-V curve near zero output current, and similarly $J_{SC}$ is determined from a linear regression to the I-V points near zero output voltage. The maximum power point $P_{MAX}$ is obtained from an at least fifth-order polynomial fit to the data points of the output power versus voltage with the constraints in which the $P_{MAX}$ must be greater than 85% of the measured maximum power and the $V_{MAX}$ must be greater than 85% of the measured $V_{MAX}$.

## Spectral Response Measurement Instrumentation and Procedures

### Spectral Response Measurement Instrumentation

Two types of measurement systems, i.e., the filter wheel and grating monochromator systems, are commonly used to measure the spectral response of the solar cells. The grating monochromator system has a basic feature of the flexibility to select wavelength, but has the disadvantages of low light intensity, poor beam uniformity, and small beam size. While the filter wheel system has the features of higher light intensity, better beam uniformity, and larger beam size, but has a drawback of limited and fixed wavelengths in spectral response measurements. With the small area of the CIS-based solar cells fabricated at University of Florida, we have constructed a spectral response measurement system using a grating monochromator to analyze the spectral response and quantum efficiency of our solar cells. The measurement system scanning the spectral range from 400 nm to 1400 nm with 10 nm as an increment step has the capability of applying white light bias and voltage bias to the test cell when the measurement is performed.

**Monochomator and monochromatic light source**

As illustrated in Figure 6-3, a 30-Watt tungsten-halogen lamp is coupled with the monochromator as a light source to produce a monochromatic light with a narrow bandwith of about 10 nm in the wavelength range from 350 nm to 2500 nm and with a resulting beam size of around 9mm×14mm on the test plane. With the considerations of the possible spatial non-uniformity of the test cell to the spectral response, significant errors arising from the test cell and reference detector with different size or shape under a non-uniform monochromatic light [75], and the potential disadvantages, namely the low light intensity, uneven light distribution, and small beam size, directly inheriting from a typical monochromator measurement system, the geometric location and selection of the optical components including the lenses, mirror, and optical diffuser are specially arranged with caution so that the entire area of the cell on the test plane is covered with a uniform and adequate illumination-level monochromatic light. The entrance slit width of the monochromator is opened to its maximum to increase the throughput of light intensity at the expense of the resulting image resolution from the output of the monochromator. The exit slit width of the monochromator is opened to around 2.8mm to keep the bandwidth of the monochromatic light at about or less than 10 nm for the wavelength from 400 nm to 1400 nm. The divergent monochromatic beam from the exit of the monochromator is collimated through the condenser lens, subsequently reflected onto the test plane via the high-reflection broadband flat mirror, and finally homogenized by a high-transmission (>85%) optical diffuser to make the monochromatic light more uniform without substantially sacrificing the light intensity.

Since there is no real-time calibration and the data of the incident power density on the test plane are stored before the photocurrent measurement, the care must be taken for the stability of the light source used for the monochromator. A stable well-regulated power supply is served as the power source for the light source of the tungsten-halogen lamp. Two order sorting filters are used to block the undesired harmonic terms from the monochromator. One with the cut-on wavelength of around 610nm and the other with the cut-on wavelength of about 830 nm are applied for the ranges of wavelength from 630 nm to 1000 nm and from 1000 nm to 1400 nm, respectively. It is not necessary to use the order sorting filter for the range of wavelength from 400 nm to 630 nm because the silicon detector, which only responses to the wavelength above 360 nm, is used as the reference detector in the measurement system.

### Monochromatic light chopper

An optical chopper used together with a lock-in amplifier in the spectral response measurement system can discriminate the chopped ac signal from the undesirable noise and strong dc signal from the bias light, and hence increases the signal-to-noise ratio in the spectral response measurement system. However, the errors can occur for the inadequate use of chopped light method when the test cell and reference detector are of different size and/or shape [76]. These errors can be minimized by locating the chopper blade in the narrowest location of the monochromatic beam pathway [76]. Therefore, we put the chopper right next to the exit of the monochromator in the measurement system to reduce the errors. In order to avoid the interference of the harmonics from the power lines of the bias light, a chopping frequency of 150Hz is used in the measurement.

**Bias light source**

Besides the monochromatic light a bias light is typically used in the spectral response measurement not only to approximate the standard operating conditions but also to compensate to effects, which might be attributed to the trapping mechanisms of the test cell, about the non-linearity of the photo-generated current in the cell to the illumination level. An ELH lamp is used as the bias light source in the measurement system. The light intensity of the ELH lamp is adjusted during the spectral response measurement, which is one hundred times greater than that of the monochromatic light, to provide the sufficient illumination level such that the short-circuit current is within 70%-100% of the $I_{SC}$ measured from the photo-I-V measurement with respect to the SRC. A screen is placed between the chopper and lens to eliminate the undesired noise, whose magnitude can be comparable to the measured ac signal due to the high illumination-level bias light, resulting form the stray light reflected from the components and the possible direct illumination from the bias light through the chopper onto the test cell.

**Spectral detector and synchronous detection instrumentation**

The NIST traceable calibrated silicon and germanium photodetectors together with a lock-in amplifier are employed to measure the incident power density of the frequency-chopped monochromatic light beam on the test plane of the measurement system. A zero-inductance four-terminal resistor of 2Ω is used as the current-voltage converter to convert the ac photocurrent generated from the photodetectors or the tested cell into the photovoltage, which is then fed into the lock-in amplifier. The monochromatic signal through the chopper becomes a trapezoidal waveform. For an absolute photocurrent measurement of the detectors, the signal measured from the lock-in amplifier must be multiplied by a waveform correction factor (i.e. multiplicative constant) because the lock-in amplifier typically measures the amplitude of fundamental component of the trapezoidal waveform (root-mean-square signal), which is not exactly the same as the peak amplitude. Since the signals for the reference detectors and test cell are measured with similar electronic instruments, all multiplicative errors are dropped out and the absolute spectral response of the test cell can then be achieved.

### Spectral Response Measurement Procedures

The monochromator, which is controlled by a computer program written in *LabVIEW* software via the interface of GPIB, scans the spectral range from 400 nm to 1400 nm with 10 nm as an incremental step. The incident power density on the test plane is first measured by the photodetectors and the data are stored in the hard disk of the computer. The spectral response measurement is operated at the short-circuit mode by adjusting the variable load in the circuit loop to set the measurement at short-circuit condition with the terminal voltage of the test cell within ±5mV. The light intensity of the light-bias lamp is adjusted such that the short-circuit current is within 70%-100% of the $I_{SC}$ measured from the photo-I-V measurement with respect to the standard reporting conditions (100 mW/cm$^2$, 25°C, and reference spectrum). The ac photocurrent $I_{\text{test cell}}(\lambda)$ of the test cell is converted into photovoltage with a zero-inductance four-terminal precision resistance and is measured by using a lock-in amplifier. Subsequently the spectral response is calculated from the data stored in the computer previously and the measured photocurrent of the test cell. The external quantum efficiency as a function of wavelength can be converted from the spectral response using the following expression:

$$\mathrm{QE}(\lambda)=\frac{\mathrm{h}\cdot\mathrm{c}\cdot\mathrm{I}_{\text{test cell}}(\lambda)}{\mathrm{q}\cdot\lambda\cdot\text{power density}_{\text{detector}}(\mathrm{W/cm^2})\cdot\text{Area}_{\text{test cell}}(\mathrm{cm^2})}\times 100\%$$

where h, c, q, and λ are the Plank constant, speed of light, electronic charge, and the photon wavelength, respectively. Figure 6-4 shows the spectral response and external quantum efficiency of a UF CIS solar cell taken by this measurement system.

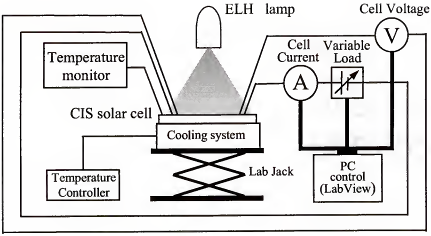

Figure 6-1. Apparatus and block diagram of I-V measurement system for the CIS-based cells.

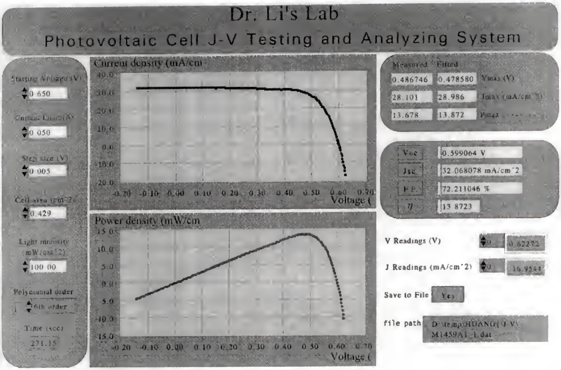

Dr. Li's Lab

Photovoltaic Cell J-V Testing and Analyzing System

Starting Voltage (V) 0 650

Current Limit (A) 0 050

Step size (V) 0 005

Cell area (cm^2) 0 429

Light intensity (mW/cm^2) 100 00

Polynomial order 1 6th order

Time (sec) 271.15

| Measured | Fitted | |
|---|---|---|
| 0.486746 | 0.478580 | Vmax (V) |
| 28.101 | 28.986 | Jmax (mA/cm^2) |
| 13.678 | 13.872 | Pmax |

Voc 0.599064 V

Jsc 32 068078 mA/cm^2

F.F. 72.211046 %

η 13 8723

V Readings (V) 0 0.62272

J Readings (mA/cm^2) 0 16.9544

Save to File Yes

file path D:\temp\HUANG\J-V\ M1459A1_1.dat

Figure 6-2. The J-V measurement and analysis for solar cells using the *LabVIEW* program. (The tested solar cell in this illustration is a CIGS solar cell fabricated by NREL.)

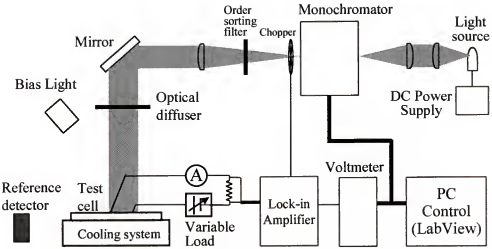

Figure 6-3. The block diagram of a spectral response measurement system for the CIS-based solar cells.

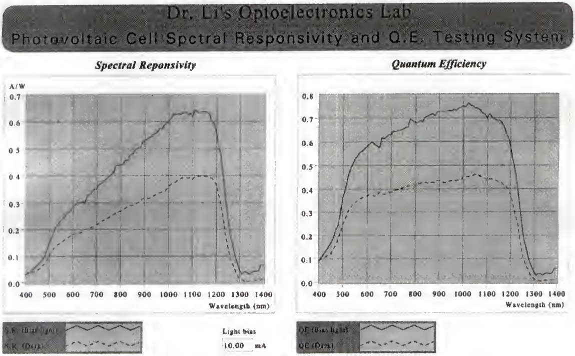

Light bias 10.00 mA

Figure 6-4. The spectral response and quantum efficiency measurements for solar cells using *LabVIEW* program. (The test cell in this illustration is a UF CIS solar cell.)

# CHAPTER 7
# DEVELOPMENT AND CHARACTERIZATION OF BUFFER LAYERS FOR COPPER-INDIUM-DISELENIDE-BASED SOLAR CELLS

## Introduction

In a typical CIGS-based solar cell a very thin CdS buffer layer (< 500Å) is usually deposited between the ZnO window layer and the CIGS absorber layer in order to achieve high conversion efficiency. Among various buffer layer materials such as CdS, (Cd,Zn)S, ZnS, $Zn(O,S,OH)_x$, ZnO, ZnSe, $In_x(OH,S)_y$, $In_2S_3$, $In(OH)_3$, $SnO_2$, $Sn(S,O)_2$, ZnSe, or $ZrO_2$ deposited by the CBD, ALE, MOCVD, or other deposition processes, the best performance CIGS solar cell with a total-area conversion efficiency of 18.8% [10] and other high-efficiency (> 17%) CIGS solar cells [77, 78] were obtained by using the CBD CdS buffer layers. However, the role of CBD CdS buffer layer on the CIGS cell performance is not well understood. In view of the ability of depositing large area and uniform films, the non-vacuum low-temperature CBD process is very advantageous for manufacturing low-cost photovoltaic devices. Although a dry vacuum process has advantages for in-line manufacturing, the CBD process provides a simple, flexible, and cost-effective means for the deposition of buffer layers on the CIS-based solar cells. It has been reported that Cd-partial electrolyte treatment [79] modifies the CIGS surface favorably as evidence by the improvement in performance of CIGS solar cells [80]. Unfortunately, the basic mechanisms responsible for the cell performance are still not clear.

Using the wider band-gap materials to replace the CdS ($E_g \approx 2.4$eV) buffer layer could improve the quantum efficiency of the CIGS cell at shorter wavelengths, resulting in an increase of the short-circuit current. The (Cd,Zn)S buffer layer has a band-gap energy greater than 2.4eV, and can provide a better lattice match to the CIGS absorber layer. On the other hand, the toxicity of cadmium (Cd) and the desirability of using a wider band-gap material to achieve a higher spectral response in the blue region have motivated the search for other alternative buffer layer materials. Using ZnS ($E_g \approx 3.6$eV) and $In(OH)_xS_y$ ($E_g \approx 2.54$eV [81]) buffer layers for the CIGS solar cells have achieved high active-area conversion efficiencies of 18.1% [82] and 15.7% [83], respectively. Thus, both ZnS and $In(OH)_xS_y$ thin films are promising candidates for the Cd-free buffer layers among the reported alternative materials

The buffer layer materials of CdS, (Cd,Zn)S, ZnS, or $In(OH)_xS_y$ was deposited on the soda-lime glass substrates, $Cu(In,Ga)Se_2$ (CIGS), or $Cu(In,Ga)(Se,S)_2$ (CIGSS) thin films by the chemical-bath-deposition (CBD) process. The impurities in the deposited films and their atomic concentration were characterized by the x-ray photoelectron spectroscopy (XPS) and auger electron spectroscopy (AES) analyses. In addition, the composition of depth profile of the samples was characterized by using the AES. The band-gap energy of the deposited $In(OH)_xS_y$ thin films was determined from the optical absorption data. Both the CIGS and CIGSS samples deposited with the CdS, (Cd,Zn)S, ZnS, or $In(OH)_xS_y$ buffer layers by the CBD process were fabricated into solar cells. The current-voltage (I-V) characteristics of these cells with the alternative buffer layers were measured, and the results were compared to the cells deposited with CBD CdS buffer layers. The results show a comparable performance among these cells, and further optimization of the deposition conditions should improve the performance of the cells deposited with the alternative buffer layers.

## Processing

### Chemical-Bath-Deposition Conditions

In the deposition of thin solid films in a chemical bath by the CBD process the nucleation centers are regularly formed by the absorption of metal hydroxo species on the surface of the substrate. The initial layer of the thin film is formed through the replacement of hydroxo group by the sulphide ions, and subsequently the solid film is grown by the condensation of metal and sulphide ions onto the top of the initial layer.

The aqueous solution consisting of $2.4\times10^{-4}$M $CdCl_2$, $2.38\times10^{-3}$M $NH_2CSNH_2$, $7.43\times10^{-4}$M $NH_4Cl$, and $6.61\times10^{-4}$M $NH_4OH$ at a bath temperature in the range of 80 to 85°C was applied for the deposition of CdS films. The CBD $In(OH)_xS_y$ films were deposited using a freshly prepared aqueous solution of 0.005M indium chloride and 0.15M thioacetamide at 70°C with deposition times varied between 15 and 25 minutes and with a pH value of 1.8. In order to avoid nucleation centers in the bath for the deposition of $In(OH)_xS_y$, the insoluble particles present in the stock solution of thioacetamide were eliminated by filtration. The complexing agent, acetic acid, was added into the bath during the deposition of $In(OH)_xS_y$ as a new deposition condition to improve the film quality. The deposition of (Cd,Zn)S buffer layers was carried out with $1.2\times10^{-3}$M $CdCl_2$, $6.27\times10^{-4}$M $ZnCl_2$, $1.2\times10^{-2}$M thiourea, $5.27\times10^{-4}$M $NH_3$, and $1.39\times10^{-3}$M $NH_4Cl$, and the bath temperature was maintained at around 85°C. For the CBD ZnS films the deposition bath was prepared with an aqueous solution of $2.5\times10^{-2}$M $ZnSO_4$,

$3.5\times10^{-2}$M thiourea, 1M $NH_3$, and 3M hydrazine at a bath temperature varied between 70 and 80°C.

Two competitive processes, namely the heterogeneous process of the solid film deposited on the substrate and the homogeneous process of precipitation in the reaction bath, took place simultaneously in the chemical bath during the CBD process. In order to remove the possible precipitation, which may be attached on the surface of the films, the substrates were well rinsed with DI water after the deposition and blown dry with nitrogen stream.

### Device Fabrication

The CdS, (Cd,Zn)S, ZnS, or $In(OH)_xS_y$ buffer layers were deposited on the CIGS and CIGSS samples provided by the Institute of Energy Conversion (IEC) of the University of Delaware, ISET, and Siemens Solar Industries. The high/low resistivity ZnO bilayer films were then deposited by either the MOCVD or sputtering technique on these samples. The Ni/Al grids as contact pads were finally deposited to obtain the finished cells.

## Characterization of CdS, (Cd,Zn)S, ZnS, and $In(OH)_xS_y$ Buffer Layers

### Compositional Analysis

The near surface composition of the CdS, (Cd,Zn)S, ZnS, and $In(OH)_xS_y$ films deposited on the soda-lime glass substrates and CIGS samples were characterized by the x-ray photoelectron spectroscopy (XPS), and the results are shown in Figure 7-1. The XPS analysis was conducted by using a Physical Electronics 5100 ESCA equipped with a Mg Kα X-ray source and a hemispherical analyzer. Depth profiling was performed with an argon ion source operating at the beam energy of 4 KeV. The charging effects were taken into account by referring the measured spectra to the binding energy peak of C 1s at 285eV. Carbon was initially present for all films deposited by the CBD process described in the previous section but became undetectable during sputter depth profiling, indicating that little carbon was incorporated in the films. Besides carbon, elements of metal (Cd, Zn, or In), sulfur, and oxygen were also identified in the deposited films.

Before and after sputtering the CBD CdS films the binding energy peaks of Cd $3d_{5/2}$ and S $2p_{3/2}$ at about 405.3eV and 161.5eV were obtained, respectively. The result shows that the sulfur peak is in good agreement with the reported data (S-Cd: 161.7eV [84]). The binding energies of Cd-S (405.3eV [84]), Cd-O (405.2eV [84]), and Cd-OH (405.0eV [84]) are too close to identify the exact compounds presented in the film from the measured Cd peak at 405.3eV. Two peaks at 529.48eV and 531.09eV obtained from the deconvolution of O 1s binding energy curve demonstrate that the film consists of chemical bonds Cd-O (529.2eV [84]) and Cd-OH (530.9-532eV [84]). The estimated atomic concentration ratios of [Cd]/[S] and [S]/[O] are approximately 1.6 and 5.4, respectively. For the (Cd,Zn)S film the atomic concentration was estimated from the peak area of each element, Cd, Zn, S, and O, in the film. The XPS result indicated that a large amount of oxygen (around 40%) and a small amount of zinc (around 2%) were incorporated in the (Cd,Zn)S film. Because the precipitation of CdS is easier and faster than that of ZnS during the CBD process, the deposited (Cd,Zn)S film only had a very small quantity of zinc even though the concentration of zinc source was an order of magnitude higher than that of cadmium source in the deposition bath.

For the ZnS film, the deconvolution of Zn $2p_{3/2}$ binding-energy spectrum from 1018eV to 1026eV revealed only one peak at 1022.0eV. This is consistent with the energy peaks of possible compounds ZnS and/or ZnO at 1022.0eV and 1021.8eV-1022.5eV [84], respectively. No evidence of $ZnSO_4$ was found from the Zn $2p_{3/2}$ peak, where the binding energy peak of $ZnSO_4$ is 1023.1eV. The oxygen 1s photoelectron binding energy spectra were fitted with Gaussian-Lorentzian curves both before and after sputtering the film. The XPS spectra can be represented by two peaks at about 530.6-530.1eV and 531.6eV, which correspond to the chemical bonds of Zn-O (530.4eV [84]) and metal-hydroxide compound (530.9-532eV [84]), respectively. Thus the results suggest that the CBD ZnS films might be a mixture of ZnS, ZnO, and $Zn(OH)_2$. The estimated atomic concentration ratio of Zn, S, and O was about 5:3:2 after sputtering the film for 4 minutes.

For the $In(OH)_xS_y$ films deposited by CBD with acetic acid in the bath, a binding energy peak of S $2p_{3/2}$ was found at about 161.24eV (see Figure 7-2), which can be assigned to the sulfide compound. In Figure 7-2, a very weak binding energy peak at around 168.96eV suggests that the indium sulfate (169-171eV [84]) was also present. After sputtering the film for 4 minutes no peak was found between 167ev and 173eV. We conclude that the sulfate compound only exists at the surface of the film. From Figure 7-3 the montage of binding energy distribution curves between 526eV and 544eV, it is evident that the shape of these curves changes for the oxygen 1s peak during the depth profiling. As shown in the inset of Figure 7-3(a), before sputtering the XPS spectra can be represented by two peaks at 531.4eV and 529.5eV, suggesting that the oxygen is present in the form of In-OH (531.8eV [84]) and In-O (529.8eV [84]). As exhibited in the inset of Figure 7-3(b), likewise two fitted peaks at 531.5eV and 530.0eV are present in the curve after sputtering the film. This suggests that the film has more indium hydroxide than indium oxide in the near surface region. The estimated atomic concentration ratios of In, O, and S were found to be around 49.9%: 26.5%: 23.6% after sputtering for 4 minutes.

To determine whether the carbon was only present at the surface or incorporated throughout the film, Auger Electron Spectroscopy (AES) sputter depth profiles were performed. Figure 7-4 shows the differential Auger spectra taken for the initial $In(OH)_xS_y$ film and compared to those taken after 3 and 5 minutes of sputtering. The results indicate that the carbon is only at the surface and likely derived from the ambient. The spectra in Figure 7-4 also show that after 5 minutes sputtering time, some regions of the glass were exposed as evidenced by the appearance of Ca and Si signals. An AES depth profile for the CIGS/$In(OH)_xS_y$ sample is shown in Figure 7-5. The results indicate that the buffer layer barely covered the CIGS layer. Although intermixing between the $In(OH)_xS_y$ and the CIGS layers is suggested from the depth profile, this result is probably attributed to the roughness of CIGS surface. Interdiffusion between the $In(OH)_xS_y$ buffer layer and the CIGS absorber layer is not expected to occur during the low temperature CBD process. However, an observation of intermixing at the interface between CdS and CIGS involving the elements of S, Se, and In was reported recently [85]. Furthermore after the completed cell processing a strong intermixing between absorber (CIGS), buffer (CdS), and TCO (ZnO) material in the interface region was found [86].

### Optical Properties

The spectral dependence of the transmittance for the $In(OH)_xS_y$ films grown on the soda-lime glass substrates was measured using a spectrophotometer, and the results are shown in the inset of Figure 7-6. The $In(OH)_xS_y$ films with shorter deposition time have a higher transmittance at shorter wavelengths, which will result in an increase of short-circuit current in the CIGS cells. The buffer layers grown with longer deposition time, however, could provide a better shield effect against the sputtering damage during the ZnO deposition step and thereby reduce the interface recombination. Thus, the buffer-layer thickness needs to be optimized for the solar-cell performance. The band-gap energy of $In(OH)_xS_y$ was determined from the optical absorption data. To obtain the direct transition, $(\alpha h\nu)^2$ was plotted against $h\nu$ for the $In(OH)_xS_y$ films as illustrated in Figure 7-6. A band-gap energy of 2.54eV was obtained from the intercept of this plot. The band-gap energy of $In(OH)_xS_y$, which depends on the films stoichiometry, lies between 2eV and 3.7eV, the band-gap energies of $In_2S_3$ and $In_2O_3$, respectively [87].

## Current-Voltage Characteristics of CIGS-Based Solar Cells with CdS, (Cd,Zn)S, ZnS, or $In(OH)_xS_y$ Buffer Layers

### CIGS-Based Cells with CdS or (Cd,Zn)S Buffer Layers

The J-V characteristics of CIGSS solar cells with the CdS or (Cd,Zn)S buffer layers deposited by our baseline CBD process are shown in Figure 7-7, where the CIGSS absorbers are provided by the Siemens Solar Industries. Evidently the CIGSS solar cell with the CdS buffer layer has the best conversion efficiency. On the contrary the performance of the other cells deposited with the (Cd,Zn)S, ZnS, or $In(OH)_xS_y$ buffer layers yields a lower conversion efficiency than that of the CIGSS/CdS cell. From the results of this study further optimization of the alternative buffer layers is needed, which includes the optimization of the deposition conditions to improve the film quality and the investigation of the effects of post-deposition annealing and light soaking on the devices.

In addition, the CdS buffer layers were also deposited by using the UF baseline CBD process [88] with a deposition time of 30 or 40 minutes on the same sets of CIGS samples provided by the IEC. The CIGS/CdS cell with a deposition time of 30 minutes has a better performance with $V_{OC}$ =0.51V, $J_{SC}$ =30.5mA/cm$^2$, F.F. =63.8%, and conversion efficiency $\eta$ =9.99%, and the results are listed in Table 6-1. Apparently, the effect of annealing considerably improves the performance of these cells with either the thinner or thicker buffer layers. Also the performance of the CIGS cells can be further enhanced by optimizing the thickness of the CdS buffer layers via the variation of the deposition time.

### CIGS-Based Cells with ZnS Buffer Layers

Figure 7-8 illustrates the effect of ZnS buffer-layer thickness on the performance of Siemens CIGSS solar cells. By increasing the ZnS buffer-layer thickness the absorption of incident light in the ZnS layer increases, and thus the short- circuit current of the cell decreases. Due to the high resistivity of ZnS buffer layer a thick buffer layer can cause a high series resistance in the solar cell and results in a poor fill factor as shown in Figure 7-8. With a higher band gap of ZnS than that of CdS, the CIGSS/ZnS cell should have a higher short-circuit current than the CIGSS/CdS cell because of the higher quantum efficiency at the shorter wavelength region. However, the highest short-circuit current obtained in this study for the CIGSS/ZnS cell was only 27.74 mA/cm$^2$ (see Figure 7-7), whereas for the CIGSS/CdS cell a short-circuit current of 31.4 mA/cm$^2$ was obtained. Thus, the further optimization of ZnS layer thickness and deposition condition is needed in order to achieve the potential of ZnS buffer layers for the CIS-based cells. The performance of the CIGS solar cells fabricated from the same set of ISET CIGS samples with our ZnS or ISET CdS buffer layers is shown in Figure 7-9. The CIGS/ZnS cell has a higher short-circuit current as expected but the cell suffers a comparably low open-circuit voltage.

### CIGS-Based Cells with $In(OH)_xS_y$ Buffer Layers

In order to obtain an optimum CBD process procedure for the deposition of $In(OH)_xS_y$ buffer layers, three different sequences of adding chemicals $InCl_3$ and $CH_3CSNH_2$, which might result in the modification of CIGS surface, were applied to the CIGS samples. It was found that the CIGS sample dipped in the DI water for a few seconds prior to the start of the deposition, which might have a precleaning effect on the CIGS surface, showed the best device performance from this experiment. The results are shown in the Table 7-2.

Each I-V measurement for the CIGS cells comprised a sweep in the $I_{SC}$ to $V_{OC}$ direction followed immediately by a sweep from $V_{OC}$ to $I_{SC}$ direction. The dark- and photo-I-V curves of the CIGS/$In(OH)_xS_y$ heterojunction cell before and after annealing at 200°C in the air for 20 minutes are shown in the Figure 7-10. As illustrated a hysteresis loop was observed in the photo-I-V curves of the CIGS/$In(OH)_xS_y$ cells before and after annealing. On the contrary, no evidence of a hysteresis loop in the photo-I-V curves of the CIGS/CdS cells was found in this study.

Initially the device without annealing showed the inflected I-V curve. As shown in Figure 7-10 and Figure 7-11, the fill factor (F.F.), $J_{SC}$, $V_{OC}$, and hence the conversion efficiency were dramatically improved after annealing time of 20 minutes. The cells, however, showed degradation when the total annealing time was increased to 40 minutes. In order to improve the cell performance, it is necessary to optimize the annealing conditions.

Comparing the performance of CIGS/CdS cells and CIGS/In(OH)$_x$S$_y$ cells, we have found that the latter has a much higher open-circuit voltage, a comparable short-circuit current density, and a very poor fill factor ($V_{OC}$ =0.57V, $J_{SC}$ =29.1mA/cm$^2$, F.F. =44.6%, and a low conversion efficiency $\eta$ =7.39%) as shown in Figure 2.12, while the CIGS/CdS cell yielded a conversion efficiency of 9.99%, $V_{OC}$=0.51V, $J_{SC}$=30.5mA/cm$^2$, and F.F.=63.8%. The possible reason why the CIGS/In(OH)$_x$S$_y$ cell has a higher $V_{OC}$ is that the net acceptor concentration in the CIGS layer is increased and hence the depletion width is reduced. The CBD alternative buffer layer process might influence the charged states at the surface or at the grain boundaries of the CIGS layer and hence modify the electrical properties of the absorber layer as well [83]. However, the CIGS/In(OH)$_x$S$_y$ cell has a lower $J_{SC}$ due to the lower quantum efficiency than the CIGS/CdS cell in the long wavelength region [83].

By adding the complexing agent of acetic acid into the chemical bath, a more adherent, reproducible, homogeneous, and higher quality In(OH)$_x$S$_y$ film [89] has been deposited on the glass substrates and Siemens CIGSS samples. The performance of one CIGSS cell deposited with In(OH)$_x$S$_y$ buffer layer using acetic acid and the performance of the CIGSS cells deposited with other buffer layers are shown in Figure 7-7. The result reveals that we can take advantage of the $In(OH)_xS_y$ buffer layer deposited by the new deposition method to improve the cell performance.

## Summary and Conclusions

A study of the electrical and optical properties of the CBD buffer layers on the soda-lime glass substrates and on the absorber layers was conducted. The XPS results indicated that CdS, (Cd,Zn)S, ZnS, and $In(OH)_xS_y$ films deposited by the CBD method were not completely pure. A small amount of carbon was found to incorporate in the first few atomic layers of the films. Also oxygen in the form of metal oxide and/or metal hydroxide was incorporated into the films during the deposition process. A better quality $In(OH)_xS_y$ buffer layer has been achieved by adding the acetic acid into the reaction bath. Annealing has been found to be a key factor for improving the conversion efficiency of CIS-based cells deposited with alternative buffer layers. Among the CIS-based solar cells with CdS, (Cd,Zn)S, ZnS, or $In(OH)_xS_y$ buffer layers studied in this work, the CIGSS/CdS cell gave the best performance. From the J-V characteristics obtained for the CIS-based solar cells with the alternative buffer layers, the deposition conditions of CBD process are merited to further optimize in order to realize the potential advantages of these buffer layers. Future study of the CIS-based solar cells with alternative buffer layers will focus on optimizing annealing conditions and on investigating the light soaking effects.

Table 7-1. The performance of CIGS Cells with CBD CdS buffer layers

| | Deposition time | As deposited | Annealing 5 min. |
|---|---|---|---|
| Conversion Efficiency $\eta$ | 40minutes | 8.87% | 9.91% |
| | 30minutes | 8.41% | 9.99% |
| Fill Factor (F.F) | 40minutes | 61.7% | 61.9% |
| | 30minutes | 60.8% | 63.8% |
| Open-circuit Voltage $V_{OC}$ | 40minutes | 0.4745V | 0.5017V |
| | 30minutes | 0.4697V | 0.5136V |
| Short-circuit Current Density $J_{SC}$ | 40minutes | 30.31 mA/cm$^2$ | 31.88 mA/cm$^2$ |
| | 30minutes | 29.47 mA/cm$^2$ | 30.51 mA/cm$^2$ |

Table 7-2. The Performance of the CIGS solar cells with CBD $In(OH)_xS_y$ buffer layers using different procedures of adding chemicals

| | Cell- 1 | Cell- 2 | Cell- 3 |
|---|---|---|---|
| Conversion Efficiency $\eta$ | 7.39 % | 5.73 % | 5.23 % |
| Fill Factor (F.F) | 44.6 % | 38.2 % | 38.3 % |
| Open-circuit Voltage $V_{OC}$ | 0.57 V | 0.52 V | 0.51 V |
| Short-circuit Current Density $J_{SC}$ | 29.1 mA/cm$^2$ | 28.9 mA/cm$^2$ | 27.0 mA/cm$^2$ |

Note: For the CBD process: cell- 1 was first immersed in DI water, and then both $InCl_3$ and $CH_3CSNH_2$ were added into the bath simultaneously; cell- 2 was first immersed in the solution of $CH_3CSNH_2$, and then $InCl_3$ was added into the bath; cell- 3 was first immersed in the solution of $InCl_3$, and then $CH_3CSNH_2$ was added into the bath.

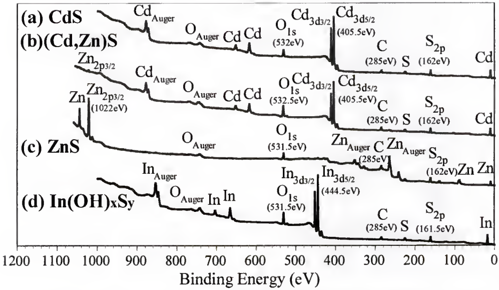

Figure 7-1. XPS spectra of CdS, (Cd,Zn)S, ZnS, or In(OH)$_x$S$_y$ thin films deposited on CIGS thin films by the CBD process.

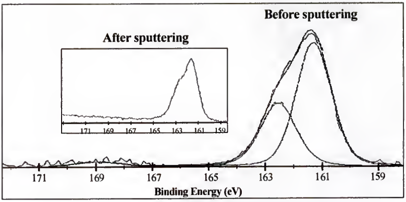

Figure 7-2. The XPS spectra of $In(OH)_xS_y$ films.

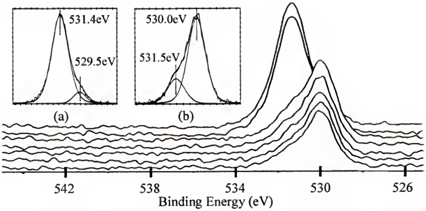

Figure 7-3. Montage of photoelectron binding energy spectra for a depth profile of an $In(OH)_xS_y$ film (View with surface curve in the background). The oxygen 1s photolectron binding energy spectra are (a) as-received surface, and (b) after sputtering for 4 minutes.

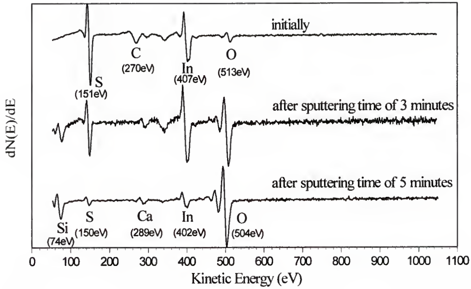

Figure 7-4. Differential Auger spectra of the $In(OH)_xS_y$ thin film deposited on the glass substrate.

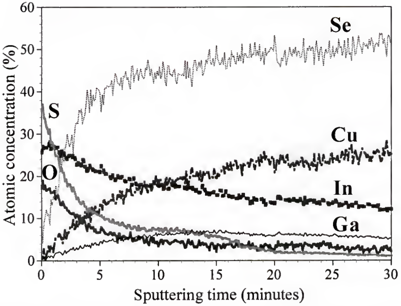

Figure 7-5. The Auger depth profile of the $In(OH)_xS_y$ thin film deposited on the CIGS cell by CBD process.

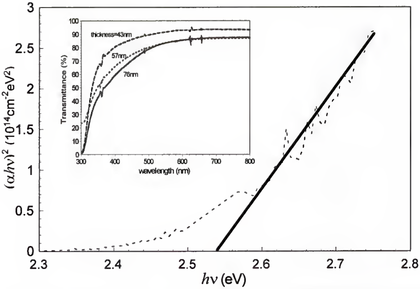

Figure 7-6. $(\alpha h\nu)^2$ versus $h\nu$ plot for the $In(OH)_xS_y$ thin film deposited on the glass substrate by the CBD process.

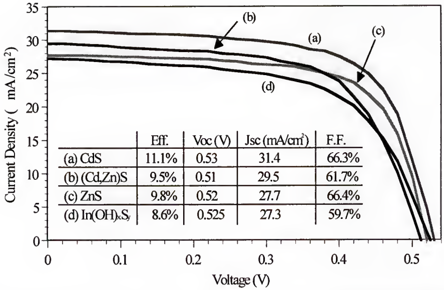

| | Eff. | Voc (V) | Jsc (mA/cm$^2$) | F.F. |
|---|---|---|---|---|
| (a) CdS | 11.1% | 0.53 | 31.4 | 66.3% |
| (b) (Cd,Zn)S | 9.5% | 0.51 | 29.5 | 61.7% |
| (c) ZnS | 9.8% | 0.52 | 27.7 | 66.4% |
| (d) In(OH)$_x$S$_y$ | 8.6% | 0.525 | 27.3 | 59.7% |

Figure 7-7. The J-V characteristics of the CIGSS cells with CdS, (Cd,Zn)S, ZnS, or In(OH)$_x$S$_y$ buffer layers.

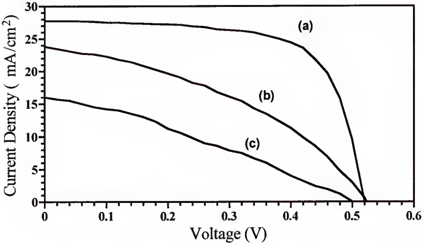

Figure 7-8. The J-V characteristics of CIGSS solar cells using different thickness of CBD ZnS buffer layers deposited for (a) 10min, (b) 20min, and (c) 25min at 70°C.

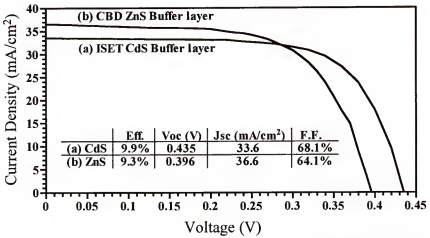

|  | Eff. | Voc (V) | Jsc (mA/cm$^2$) | F.F. |
|---|---|---|---|---|
| (a) CdS | 9.9% | 0.435 | 33.6 | 68.1% |
| (b) ZnS | 9.3% | 0.396 | 36.6 | 64.1% |

Figure 7-9. The J-V characteristics of CIGS cells with CdS buffer layer deposited at ISET or the ZnS buffer layer deposited at UF.

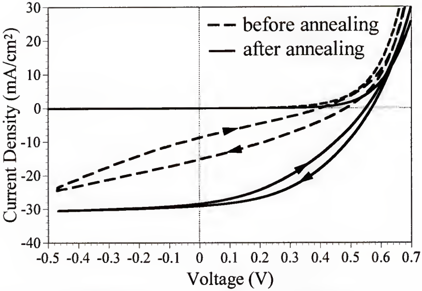

Figure 7-10. The J-V characteristics of the CIGS cell deposited with CBD $In(OH)_xS_y$ buffer layer before and after annealing.

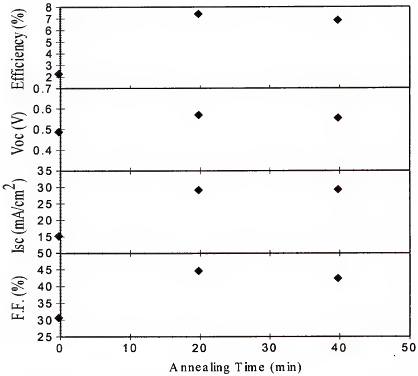

Figure 7-11. The performance of the CIGS solar cells deposited with CBD $In(OH)_xS_y$ buffer layers as a function of annealing time.

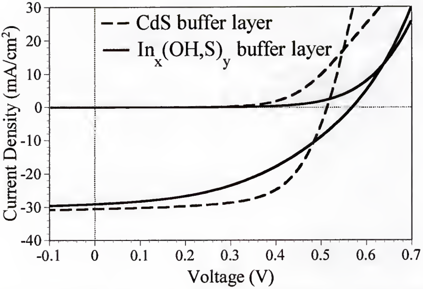

Figure 7-12. J-V characteristics of the CIGS cells with CBD- CdS or CBD-In(OH)$_x$S$_y$ buffer layer (CIGS/CdS solar cell: Eff.=9.99%, $V_{OC}$=0.51V, $J_{SC}$=30.5mA/cm$^2$, F.F.=63.8%; CIGS/In(OH)$_x$S$_y$ solar cell: Eff.=7.39%, $V_{OC}$=0.57V, $J_{SC}$=29.1mA/cm$^2$, F.F.=44.6%).

# CHAPTER 8
# DEVICE MODELING AND SIMULATION OF COPPER-INDIUM-DISELENIDE-BASED SOLAR CELLS

## Introduction

Increasing the open-circuit voltage ($V_{OC}$) to improve the overall performance of CIGS cells is highly desirable to minimize the interconnection loss in the manufacture of CIGS solar cell modules. By alloying the $CuInSe_2$ with Ga to form the $CuIn_xGa_{1-x}Se_2$ (CIGS) films, the higher band-gap energy of CIGS absorber layers can potentially better match the solar spectrum and increase the $V_{OC}$ of the fabricated cells at the expense of a reduction in the value of short-circuit current density $J_{SC}$. Using a spatial variation of Ga content within the CIGS layer, the band-gap profile can be optimized to increase the photon absorption and carrier diffusion and to reduce the recombination rate, and hence improve the $V_{OC}$ and $J_{SC}$ in the CIGS cells. Thus, the band-gap engineering of CIGS cells implemented by controlling the spatial distribution of Ga content in the absorber layer can be used to enhance the overall cell performance. A systematic computer simulation is conducted to analyze the impacts of various band-gap profiles of the CIGS layers on the performance parameters of the cells.

Schmid *et al.* [25] have demonstrated the existence of an In-rich *n*-type surface layer, which was identified as an ordered vacancy compound (OVC) and tentatively assigned the stoichiometry $CuIn_2Se_{3.5}$ or $CuIn_3Se_5$. A junction model was proposed that consists of a chalcopyrite/defect chalcopyrite heterojunction between the *p*-type bulk CIS and *n*-type OVC layers. The electrical characteristics of low hole mobilities ($\mu_n \leq 10 cm^2/V$-s), high resistivity ($10^5$-$10^6 \Omega cm$), and low carrier densities ($10^{11}$-$10^{12} cm^{-3}$) was proposed for the defect chalcopyrite $Cu(In_{1-x}Ga_x)_3Se_5$ materials for 1>x>0 [90]. Furthermore, the conductivity type changes from *n*- to *p*-type when the Ga content exceeds 30% [90]. In contrast, some literatures [91, 92] revealed that the compound of In-rich surface layer might not be the OVC and used a more general term 'surface defect layer' for this thin n-type layer on the surface of the as-deposited CIGS films. The inverted surface layer is considered to be beneficial to the performance of CIGS cells because the electrical junction is shifted away from the high-recombination interface between the CdS and CIGS absorber layers and hence the recombination rate is reduced. However, the properties of the surface defect layer such as high defect densities and high resistivity might lead to deteriorate the cell performance. In order to have a better understanding of the effects of the surface defect layer on the cell performance, the simulations with the variables of thickness, carrier mobility, and carrier density for the surface defect layer are conducted to analyze the device performance.

In this chapter, a comprehensive device modeling and numerical simulation of the performance of $Cu(In,Ga)Se_2$ (CIGS) solar cells with an emphasis on band-gap engineering of the CIGS absorber layers are carried out using the AMPS-1D (Analysis of Microelectronic and Photonic Structures) device simulation program [93]. A variety of graded band-gap structures including back surface grading and double grading of the CIGS absorber layers are examined. The device physics and performance parameters of the absorber layer structures with different band-gap profiles are analyzed. Based on the simulation results, an optimal graded band-gap structure for the CIGS cell is proposed. Additionally, the dependence of performance parameters for the CIGS cells on the existence, carrier mobility, carrier density, and thickness of the Cu-poor surface defect layer on the CIGS absorber layers are also investigated.

### Simulation of Copper-Indium-Diselenide-Based Solar Cells

The CIGS solar cell structure used in this simulation consists of the ZnO, CdS, high-recombination interface, inverted surface layer (or OVC), and the CIGS absorber. The computer simulation tool AMPS-1D is employed by specifying the semiconductor parameters in each defined layer of the cell structure as input parameters in the simulation. In view of a limited knowledge of the semiconductor parameters in each layer and uncertainties in the interface and junction properties arising from possible interdiffusion and reaction during the cell processing, the division of the layers for the cell structure is limited to a simplified device structure as depicted above. The schematic energy band diagram under equilibrium condition for a typical CIGS/CdS/ZnO solar cell with a uniform band-gap is illustrated in Figure 8-1. To proceed with the simulation, the reasonable material parameters are employed. Although no attempt was made to match the simulation results with the experimental data, the intention is to analyze the trend in the performance of CIGS cells versus the band gap parameters, spatial profiles in the CIGS absorber layers, and material parameters in the inverted surface layers.

In the simulations except otherwise mentioned, an inverted surface layer with a thickness of 30nm, electron mobility $\mu_n$=10cm$^2$/V-s, net carrier density n=10$^{12}$cm$^{-3}$, band-gap energy $E_g$=1.3eV is inserted between the CdS and CIGS layer, and an interfacial layer with a high density of effective recombination centers is placed at the metallurgical junction between the CIGS surface layer and CdS layer. The total thickness of the absorber layer is maintained at $2\mu m$ for all cases including the various graded band-gap structures studied. A deep level defect is placed in the middle of the band gap as an effective recombination center for the interface, CdS layer, and the space charge region (SCR) in the CIGS absorber. The changes in the physical properties of CIS films with the addition of Ga include an increase in band gap energy, which mainly shifts the position of the conduction band minimum [94], and changes in the hole concentration [95], bulk defect densities [96], absorption coefficients, and electron affinities. The room temperature mobility was found to remain nearly constant while varying the Ga content over a wide range [95]. To examine the effects of band gap gradient on the device performance, most of the material parameters used in the simulations are maintained unchanged except that the band gap energies, electron affinities, and optical absorption coefficients are varied with Ga mole fraction in the CIGS films.

## Results and Discussion

### Impacts of Graded Band-gap on Performance of CIGS Solar Cells

From the simulation results of the uniform band-gap CIGS cells shown in Table 8-1, it is found that the $CuIn_{1-x}Ga_xSe_2$ cell ($x \approx 0.32$ for $E_g \approx 1.2$ eV [97]) has a higher $V_{OC}$ and a smaller $J_{SC}$ than a CIS absorber stoichiometry due to the smaller absorption coefficients and the reduction in the absorption of longer wavelength photons. However, the device performance was degraded when the Ga content in the $CuIn_{1-x}Ga_xSe_2$ films exceeds 30 - 40% ($x > 0.3$-$0.4$) [98].

The recombination rate in the space charge region (SCR), which controls the $V_{OC}$ of CIGS cells, can be reduced by increasing the barrier height via the increase of band-gap energy in the SCR to improve the $V_{OC}$, but a small loss of $J_{SC}$ might be expected if the wider band-gap region is not sufficiently thin. The dependence of $V_{OC}$ on the band gap energy in the SCR of CIGS cells has been reported [99]. In the simulations, the wider band-gap CIGS layers from the highest band-gap energies of 1.16 to 1.35eV decreasing linearly to 1.04eV are placed entirely in the SCR, and the band-gap energies of the inverted layer and the remaining region of the CIGS layer are maintained at $E_g = 1.3$eV and 1.04eV, respectively. The simulation results are shown in Figure 8-2. Comparing the performance of the uniform band-gap CIS solar cells in Table 8-1, the value of $V_{OC}$ is improved without significantly decreasing the $J_{SC}$ and increases with increasing band-gap energy in the SCR. The change in the fill factor (F.F.) is related to the conduction band offset between the inverted layer and the CIGS layers.

A quasi-electrical field [100] can be established by the band-gap gradient with the incorporation of a high Ga content in the back region (near the Mo contact) of the CIGS absorber layers. The established back surface field can reduce the back surface recombination and increase the effective minority-carrier diffusion length. This results in an efficient carrier collection in the CIGS cells, and thus both the $V_{OC}$ and $J_{SC}$ are enhanced. Consequently, a back surface field (BSF) is formed by the normal grading, in which the band-gap energy is linearly increased towards the back, and the step grading, in which a wider band-gap layer is placed in the back, as illustrated in the band structures of case-2 and 3 in Table 8-2, respectively. Comparing the performance of the cells in case-1, both the $J_{SC}$ and $V_{OC}$ with either a normal- or step-back surface grading are improved simultaneously, and hence the conversion efficiency is also increased as shown in Table 8-2. Comparing the performance of the cells in cases-5 and 6 with that in case-4, the same trend was obtained again.

Besides that the simulations for the changes of band-gap near the SCR and back contact region, the effects of variation of band-gap energy in the middle region of absorber layers are investigated as well. The investigated band diagram of the CIGS cells is illustrated in Figure 8-3. The band-gap energy $E_g$ in the middle region of the CIGS cell is varied from 1.04eV to 1.18eV. The results are shown in Table 8-3. It is found that the open-circuit voltage still increased with the increased band-gap energy in this middle region. Same reasons for the uniform band-gap cells, we observe that the short-circuit current decreases with the increased band-gap energy. From the simulation results, the optimal band-gap energy in the middle region for a double grading CIGS cell is around 1.16eV.

From the simulation results, it has been found that a proper band-gap grading with a wider band-gap CIGS layer in the SCR and a back surface grading are capable of significantly improving the performance of the CIGS cells by applying the gradient of Ga content in the absorber layers. In our simulations, the band-gap energies in the SCR and back region and the thickness of the back surface grading layers are varied to achieve the optimal performance in terms of reducing the carrier recombination and increasing the carrier collection for the given material parameters and device structures. The results are shown in Table 8-2. Comparing the performance between the uniform band-gap cell (case 1 in Table 8-2) and the graded band-gap cells (case 5 and 6 in Table 8-2), the benefit of band-gap grading for the CIGS solar cells is clearly demonstrated.

## Impacts of Inverted Surface Layer on Performance of CIGS Solar Cells

The Cu-deficient region at the CIGS films surface with a high density of dislocations was estimated to have a thickness in the range of 150-300nm [101, 102]. The effects of the thickness of the inverted surface layer on the performance of the CIGS solar cells are investigated. A uniform band-gap profile with the band-gap energy of 1.16eV is employed for the CIGS layers in the simulations. The results are given in Figure 8-4. Basically, the performance of the cells with a thin inverted surface layer is superior to that of the cell without an inverted surface layer. The conversion efficiency of the cells increases with increasing thickness of the inverted surface layer but starts to drop when the thickness of the inverted layer is greater than 150nm due to the properties of low carrier densities and high densities of recombination centers for the inverted layer. With the existence of the weakly *n*-type surface layer in the CIGS cells, the beneficial effects include the reduction of recombination rate and enhancement of the carrier collection efficiency by shifting the electrical junction away from the high-recombination hetero-interface between the CdS and the inverted surface layer. Moreover, with the wider band-gap of the inverted layer than that of the CIGS layer existing between the CdS and CIGS layer, the recombination rate at the hetero-interface region is further decreased due to the enlargement of valence band offset created by the increased recombination barrier between the Fermi level and the valence band maximum. Thus, both the $J_{sc}$ and $V_{oc}$ are improved. Although the weakly n-type surface layer can benefit the performance of CIGS cells as explained above, the thicker inverted layer with material properties such as low carrier density, high resistivity, low carrier mobility, and high density of recombination centers could worsen the device performance as shown in Fig. 8-4.

The effects of varying the carrier mobility in the inverted surface layer on the device performance are investigated by varying the electron and hole mobility from 1 to 100cm$^2$/V-s, respectively. The results are summarized in Table 8-4. No profound effect on the device performance was found for the change of electron mobility in the range of study. However, the effect of changing the hole mobility on the device performance parameters such as fill factor, and hence the conversion efficiency, is evident. When the hole mobility is lower than a threshold value (e.g., 5cm$^2$/V-s) for a given condition in the simulations, there is a strong dependence of the value of hole mobility on the device performance.

An increment in the carrier density of the high-resistivity layer around the junction is expected to increase the fill factor of the cells. However, increasing carrier density in the n-type layer is usually accompanied by a reduction in the width of SCR in the p-type absorber side, and hence the carrier collection efficiency is reduced. The carrier density of the n-type inverted surface layer with a fixed thickness of 150nm is used as a variable in the simulations to study how the carrier density affects the device performance. The results show that the performance parameters for carrier densities varied from $10^{10}$ to $10^{16}$ cm$^{-3}$ are nearly the same. This could be attributed to the fact that thickness of the layer is only 150 nm. Thus, the variation of carrier density in the inverted layer does not have a significant effect on the device performance.

## Summary

The device modeling and numerical simulations of the CIGS solar cells with various absorber band-gap profiles have been carried out using the AMPS-1D program. A detailed analysis of the graded band-gap structures for the CIGS solar cells has been presented. The band-gap grading using a wide band-gap layer in the SCR and/or the back surface grading by using the gradient of Ga content in the CIGS absorber layer can greatly improve the performance of CIGS solar cells. Additionally, the effects of thickness, material properties such as carrier mobility and carrier density in the inverted surface layer on the performance parameters of CIGS solar cells are studied. The benefits of the inverted surface layer on the device performance are clearly shown. The variation in certain material parameters can significantly affect the device performance.

Table 8-1. Simulated performance parameters of the CIS ($E_g$=1.04eV) and $CuIn_{0.68}Ga_{0.32}Se$ ($E_g$≈1.2eV) solar cells with a uniform absorber band-gap profile.

| $E_g$ (eV) | $\eta$ (%) | $V_{OC}$ (mV) | $J_{SC}$ (mA/cm$^2$) | F.F. (%) |
|---|---|---|---|---|
| 1.04 | 13.00 | 500 | 38.01 | 68.4 |
| 1.20 | 15.77 | 655 | 32.27 | 74.6 |

Table 8-2. Simulated performance parameters of the CIGS solar cells with various absorber band-gap profiles.

| | Band-gap profile | $\eta$ (%) | $V_{OC}$ (mV) | $J_{SC}$ (mA/cm$^2$) | F.F. (%) |
|---|---|---|---|---|---|
| case 1 | 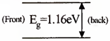 | 15.42 | 617 | 34.05 | 73.4 |
| case 2 | 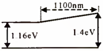 | 15.72 | 622 | 34.61 | 73.1 |
| case 3 | 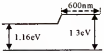 | 15.81 | 620 | 34.77 | 73.3 |
| case 4 | 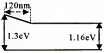 | 17.57 | 658 | 33.55 | 79.6 |
| case 5 | 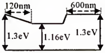 | 18.34 | 669 | 34.46 | 79.6 |
| case 6 | 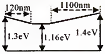 | 18.39 | 675 | 34.31 | 79.4 |

Table 8-3. Dependence of band-gap energy $E_g$ on performance of CIGS cells with a band structure as Figure 8-3.

| $E_g$ (eV) | $\eta$ (%) | $V_{OC}$ (mV) | $J_{SC}$ (mA/cm$^2$) | F.F. (%) |
|---|---|---|---|---|
| 1.04 | 16.6 | 559 | 38.2 | 77.9 |
| 1.08 | 17.4 | 595 | 37.1 | 79.0 |
| 1.12 | 17.9 | 630 | 35.9 | 79.3 |
| 1.14 | 18.0 | 646 | 35.1 | 79.1 |
| 1.16 | 18.3 | 669 | 34.5 | 79.6 |
| 1.18 | 18.2 | 684 | 33.6 | 79.3 |

Table 8-4. Dependence of electron and hole mobilities in the inverted surface layers on the simulated performance parameters of the CIGS solar cells

| $\mu_n$ (cm$^2$/V-s) | $\eta$ (%) | $V_{OC}$ (mV) | $J_{SC}$ (mA/cm$^2$) | F.F. (%) |
|---|---|---|---|---|
| 1 | 16.10 | 637 | 33.88 | 74.5 |
| 5 | 16.59 | 635 | 33.95 | 76.9 |
| 10 | 16.65 | 635 | 33.98 | 77.2 |
| 20 | 16.69 | 635 | 33.99 | 77.3 |
| 50 | 16.71 | 635 | 34.01 | 77.4 |
| 100 | 16.72 | 635 | 34.02 | 77.4 |
| $\mu_p$ (cm$^2$/V-s) | $\eta$ (%) | $V_{OC}$ (mV) | $J_{SC}$ (mA/cm$^2$) | F.F. (%) |
| 1 | 12.70 | 624 | 32.64 | 62.4 |
| 5 | 15.40 | 631 | 33.66 | 72.5 |
| 10 | 16.08 | 633 | 33.83 | 75.0 |
| 20 | 16.50 | 635 | 33.93 | 76.6 |
| 50 | 16.78 | 636 | 34.01 | 77.6 |
| 100 | 16.89 | 636 | 34.04 | 78.0 |

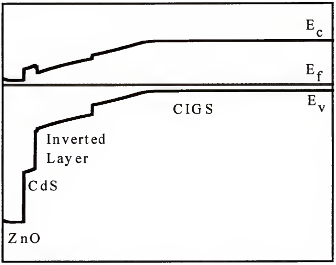

Figure 8-1. The schematic energy band diagram of a typical ZnO/CdS/CIGS solar cell under equilibrium condition.

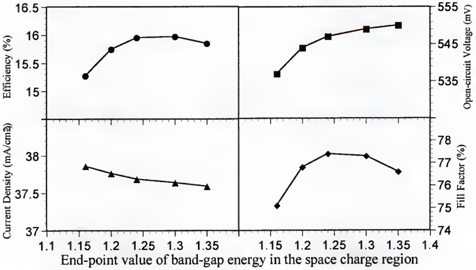

Figure 8-2. The dependence of cell performance parameters on the band-gap energy in the space charge region (SCR) of CIGS cells

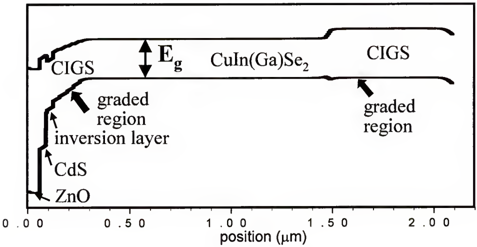

Figure 8-3. Band diagram of the CIGS cells with double grading.

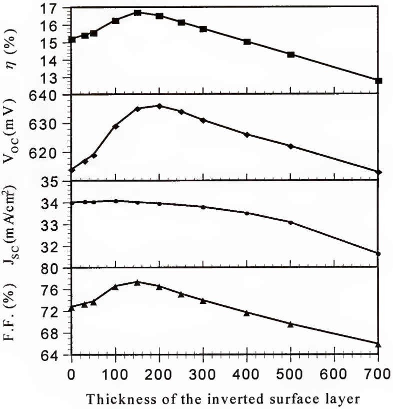

Figure 8-4. Performance parameters of the CIGS ($E_g$=1.16eV) solar cells with the inverted surface layer in varied thickness.

# CHAPTER 9
# SUMMARY AND FUTURE STUDIES

## Summary and Conclusions

The effects of CdS buffer-layer processes on the excess carrier lifetimes in the CIGS films have been investigated by using the reflection mode DBOM technique. Some conclusions can be drawn from this investigation. The formation of CdS buffer layer increases the excess carrier lifetimes for all as-grown, DI water-rinsed, S- and Cd-partial electrolyte-treated CIGS films but decreases lifetimes for the Ar-plasma cleaned samples. Buffer layers increase the excess carrier lifetimes less for the DI water-rinsed, S- and Cd-partial electrolyte-treated CIGS samples than for the as-grown samples. Especially, the sputtering of CdS buffer layer dramatically increases the excess carrier lifetimes for the as-deposited, water- and Cd-partial electrolyte-treated CIGS samples. The excess carrier lifetimes measured by the DBOM technique show the consistent trends for the CIGS samples prepared by several laboratories.

The fabrication process for the laboratory-size cells has been described. A detailed discussion on the characterization systems of current-voltage and spectral response measurements for the CIS-based solar cells is depicted as well.

For the study of the buffer layers, the composition results indicated that the films deposited by the CBD process are not pure. Oxygen in the form of metal oxide and/or metal hydroxide was usually incorporated into the films. Annealing is a key factor for improving the performance of CIS-based cells deposited with the alternative buffer layers. A better quality $In(OH)_xS_y$ buffer layer has been achieved by adding the acetic acid into the reaction bath. The performance of CIGS cells with this $In(OH)_xS_y$ buffer layer was improved. Although a higher short-circuit current density was achieved for the CIGS/ZnS cell than for the CIGS/CdS cell, the CIGS/CdS cell still gave the best performance among the buffer layers studied in this research.

The analysis of the graded band-gap profiles for the CIGS solar cells has been conducted by using the simulation program AMPS-1D. The band-gap grading using a wide band-gap layer in the SCR and/or the back surface grading by using a gradient of Ga content in the CIGS absorber layer can greatly improve the performance of CIGS solar cells. In addition, the impacts of thickness, material properties such as carrier mobility and carrier density in the inverted surface layer on the performance parameters of CIGS solar cells were investigated. The benefits of the inverted surface layer on the device performance were presented.

## Future Studies

Boron implantation into silicon substrates is the simplest way to produce p-type junctions for silicon integrated circuits. Undesirable boron clustering, defect evolution, and damage to the lattice, however, occur during the implant. Silicon wafers typically are annealed using rapid thermal annealing (RTA) to activate the boron and remove the damage created by the implant. The non-melt laser annealing (NLA) process, with its significantly greater temperature ramp rate ($>10^{12}$ C/sec), has been shown to dramatically affect the defect density in annealed Si. It has been reported that a boron-implanted silicon wafer treated with NLA and possibly RTA does not experience significant changes in the boron doping profile. But the NLA-processed silicon wafers yield material with a lower sheet resistance and a higher carrier mobility than wafers treated with only RTA or non-treated wafers. These results have suggested that NLA applied to an absorber-layer/buffer-layer stack should decrease the density of interface states at both the metallurgical and electrical junctions, as well as in the bulk material near the junction. A decrease in recombination centers leading to an increase in efficiency of solar cells is expected for the cells treated with laser annealing.

The motivation of searching for thealternative buffer layers has been discussed in Chapter 7. The primary objective of the proposed future study is to optimize the chemical bath deposition process for the growth of alternative buffer layers and provide the Cd-free buffer layers for the high-efficiency CIS-based solar cells. The zinc oxide with a band-gap energy of 3.3eV, which can potentially increase the short-circuit current of CIS-based solar cells, is also an attractive alternative to CdS for the wide band-gap n-type buffer layer. Due to the same material used as the widow layers, the CBD ZnO buffer layer could be favorable for the fabrication of Cd-free CIS-based solar cells. Although the CIGS solar cells with ZnO buffer layers deposited by the MOCVD or atomic layer deposition (ALD) method have reached the conversion efficiency of about 14% [103, 104], the fabricated CIS solar cells with CBD-ZnO thin films as buffer layers achieved around 10% which was comparable to the conversion-efficiency 12% control cell with a structure of ZnO/CdS/CIS/Mo [105]. Therefore the ZnO thin films deposited by the CBD method can be a viable replacement for the CdS buffer layer in the fabrication of CIS-based solar cells.

The ultimate goal of the following proposed task is to understand the basic recombination mechanisms, defects, and interface properties in the CIGS films and to correlate these measured recombination parameters with the processing parameters so that the device-quality CIGS films can be prepared for the high-efficiency photovoltaic applications. Current-voltage and capacitance characterization techniques will be employed for this research task. One of the most viable diagnostic tools to analyze the junction mechanisms is the current-voltage measurements. The efficiency loss due to the excess forward current and diminished photo-generated current can be determined from the measured I-V curves. With the investigation of the transport properties, a CIS-based cell model to interpret both the dark- and photo-I-V characteristics could be developed. In addition to I-V measurements, capacitance studies of p-n junction CIS-based solar cells can give a further understanding for the electronic structure of the junction region. The investigation of capacitance associated with the depletion width of the p-n junction will provide a detailed information about the concentrations and features of electrically active centers in the interface and in the CIS absorber layers. The capacitance-frequency (C-F), capacitance-voltage (C-V), capacitance-time (C-t), and current-voltage (J-V) measurements can be used as the diagnostic tools to study defect states and the junction quality of CIS-based solar cells. The density of extraneous states at the Fermi level in the depletion region, depth and number of defects or traps at the CIGS/CdS interface, and width of the intrinsic layer can be extracted from these measurements. The study of the admittance measurements on CIS-based solar cells can also be carried out to obtain more information about the electrically active defect states near the junction of the devices.

# REFERENCES

[1] S. Wanger, J.L. Shay, P. Migliorato, and H.M. Kasper, Applied Physics Letters, Vol. 25, pp. 434, 1974.

[2] L.L. Kazmerski, F.R. White, and G.K. Morgan, Applied Physics Letters, Vol. 29, pp. 268-270, 1976.

[3] R.A. Mickelsen and W.S. Chen, Conference Record of 15th IEEE Photovoltaic Specialists Conference, pp. 800-804, 1981.

[4] R.A. Mickelsen and W.S. Chen, Conference Record of 16th IEEE Photovoltaic Specialists Conference, pp. 781-785, 1982.

[5] R.R. Potter, C. Eberspacher, and L.B. Fabick, Conference Record of 18th IEEE Photovoltaic Specialists Conference, pp. 1659-1664, 1985.

[6] W.S. Chen, J. M. Stewart, B.J. Stanbery, W.E. Devaney, and R.A. Mickelsen, Conference Record of 19th IEEE Photovoltaic Specialists Conference, pp. 1445-1447, 1987.

[7] T. Walter, A. Content, K.O. Velthaus, H.W. Schock, Solar Energy Materials and Solar Cells, Vol. 26, pp. 357-368, 1992.

[8] K. Mitchell, C. Eberspacher, J. Ermer, and D. Pier, Conference Record of 20th IEEE Photovoltaic Specialists Conference, pp. 1384-1389, 1988.

[9] A. Gabor, J.R. Tuttle, D.S. Albin, M.A. Contreras, and R. Noufi, Applied Physics Letters, Vol. 65, pp. 198, 1994.

[10] M. Contreras, B. Egass, K. Ramanathan, J. Hiltner, A. Swartzland, F. Hasoon, and R. Noufi, Progress in Photovoltaics, Vol. 7, pp. 311, 1999.

[11] J.S. Ward, K. Ramanathan, F.S. Hasoon, T. J. Coutts, J. Keane, M.A. Contreras, T. Moriarty, R. Noufi, Progress in Photovoltaics, Vol. 10, pp. 41-46, 2002.

[12] T. Negami, S. Nishiwaki, Y. Hashimoto, N. Kohara, and T. Wada, Second World Conference on Photovoltaic Solar Energy Conversion, pp. 1181-1184, 1998.

[13] N. Romeo, G. Sbeneqlieri, L. Tarricone, and C. Paoroci, Applied Physics Letters, Vol. 30, No. 2, pp. 108-110, 1977.

[14] S. Wagner and P.M. Bridenbaugh, Journal of Crystal Growth, Vol. 39, No. 1, pp. 151-159, 1977.

[15] M. Saad, H. Riazi, E. Bucher, M.Ch. Lux-Steiner, Applied Physics A, Vol. 62, pp. 181-185, 1996.

[16] V. Nadenau, D. Hariskos, H.W. Schock, Proceedings of 14th E.C. Photovoltaic Solar Energy Conference, pp. 1250, 1997.

[17] R. Klenk, R. Mauch, R. Schäffler, D. Schmid, and H.W. Schock, Conference record of 22nd IEEE Photovoltaic Specialists Conference, pp. 1071-1076, 1991.

[18] V. Nadenau, U. Rau, A. Jasenek, and H.W. Schock, Journal of Applied Physics, Vol. 87, No. 1, pp. 584-593, 2000.

[19] M.E. Beck, T. Weiss, D. Fischer, S. Fiechter, A. Jäger-Waldau, M.Ch. Lux-Steiner, Thin Solid Films, Vol. 361-362, pp. 130-134, 2000.

[20] M.E. Nell and A.M. Barnett, IEEE Transactions on Electron Devices, Vol. ED-34, no. 2, pp. 257-266, 1987.

[21] D. Braunger, Th. Durr, D. Hariskos, Ch. Koble, Th. Walter, N. Wieser, and H.W. Schock, Conference record of 25th IEEE Photovoltaic Specialists Conference, pp. 1001-1004, 1996.

[22] D. Braunger, D. Hariskos, T. Walter, and H.W. Schock, Solar Energy Materials and Solar Cells, Vol. 40, pp. 97-102, 1996.

[23] R. Herberholz, V. Nadenau, U. Rühle, C. Köble, H.W. Schock, and B. Dimmler, Solar Energy Materials and Solar Cells, Vol. 49, pp. 227-237, 1997.

[24] K. Ramanathan, H. Wiesner, S. Asher, D. Niles, R.N. Bhattacharya, J. Keane, M.A. Contreras, and R. Noufi, Second World Conference on Photovoltaic Solar Energy Conversion, pp. 477-481, 1998.

[25] Schmid, D., M. Ruckh, F. Grunwald, and H.W. Schock, Journal of Applied Physics, Vol. 73, No. 6, p. 2902-2909, 1992.

[26] C. Heske, D. Eich, R. Fink, E. Umbach, T. van Buuren, C. Bostedt, L.J. Terminello, S. Kakar, M.M. Grush, T.A. Callcott, F.J. Himpsel, D.L. Ederer, R.C.C. Perera, W. Riedl, F. Karg, Applied Physics Letters, Vol. 74, pp. 1451-1453, 1999.

[27] T. Nakada and A. Kunioka, Applied Physics Letters, Vol. 74, pp. 2444-2446, 1999.

[28] U. Rau and M. Schmidt, Thin Solid Films Vol. 387, pp. 141-146, 2001.

[29] L. Stolt, M. Bodegård, J, Hedström, J. Kessler, M. Ruckh, K.O. Velthaus, and H.-W. Schock, 11th E.C. Photovoltaic Solar Energy Conference, pp. 120-123, 1992.

[30] E.D. Jackson, Transactions - Conference on the use of solar energy – the Scientific basis, University of Arizona, Vol. 5, pp. 122-126, 1955.

[31] D. Trivich and P.A. Flinn, Solar Energy Research, Madison, Editors: F. Daniels and J.A. Duffie, pp. 143-147, 1955.

[32] G.A. Landis and N. Pearsall, Conference record of 19th IEEE Photovoltaic Specialists Conference, pp. 1435-1440, 1987.

[33] M.E. Nell and A.M. Barnett, IEEE Transactions on Electron Devices, Vol. ED-34, No. 2, pp. 257-266, 1987.

[34] S.R. Kurtz, P. Faine, and J.M. Olson, Journal of Applied Physics, Vol. 68, No. 4, pp. 1890-1895, 1990.

[35] J.C.C. Fan, B-Y. Tsaur, and B.J. Palm, Conference record of 16th Photovoltaic Specialists Conference, pp. 692-701, 1982.

[36] H. Takakura, Japanese Journal of Applied Physics, Part 1, Vol. 31, No. 8, pp. 2394-2399, 1992.

[37] A.M. Bedair, S.B. Phatak, and J.R. Hauser, IEEE Transactions on Electron Devices, Vol. ED-27, No. 4, pp. 822-831, 1980.

[38] M.F. Lamorte and D.H. Abbott, IEEE Transactions on Electron Devices, Vol. ED-27, No. 1, pp. 231-249, 1980.

[39] J.A. Hutchby, R.J. Markunas, M.L. Timmons, P.K. Chiang, and S.M. Bedair, Conference record of 18th Photovoltaic Specialists Conference, pp. 20-27, 1985.

[40] J.J. Loferski, Conference record of 16th Photovoltaic Specialists Conference, pp. 648-654, 1982.

[41] M.F. Lamorte and D. Abbott, Conference record of 13th Photovoltaic Specialists Conference, pp. 692-701, 1978.

[42] L.M. Frass and R.C. Knchtli, Conference record of 13th Photovoltaic Specialists Conference, pp. 886-891, 1978.

[43] A. Martí and G.L. Araújo, Solar Energy Materials and Solar Cells, Vol. 43, pp. 203-222, 1996.

[44] M.W. Wanlass, K.A. Emery, T.A. Gessert, G.S. Horner, C.R. Psterwald, and T.J. Coutts, Solar Cells, Vol. 27, pp. 191-204, 1989.

[45] N.A. Gokcen and J.J. Loferski, Solar Energy Materials, Vol. 1, No. 3-4, pp. 271-286, 1979.

[46] R.K. Jain and D.J. Flood, Transactions of the ASME, Vol. 115, pp. 106-111, 1993.

[47] J.L. Gray, Conference record of 21st IEEE Photovoltaic Specialists Conference, pp. 345-347, 1990.

[48] R.J. Schwartz and J.L. Gray, Conference record of 26th IEEE Photovoltaic Specialists Conference, pp.871-874, 1997.

[49] J. Hou, S.J. Fonash, M. Ghosh, J. Xi, T. Liu, and F. Kampas, Conference record of the First World Conference on Photovoltaic Solar Energy Conference, pp. 445-448, 1995.

[50] S. Bae and S.J. Fonash, Conference record of the First World Conference on Photovoltaic Solar Energy Conference, pp. 484-487, 1994.

[51] P.V. Meyers, C.H. Liu, L. Russell, V. Ramanathan, R.W. Birkmire, B.E. McCandless, and J.E. Phillips, Conference record of 20th IEEE Photovoltaic Specialists Conference, pp. 1448-1451, 1988.

[52] K. Mitchell, C. Eberspacher, J. Ermer, and D. Pier, Conference record of 20th IEEE Photovoltaic Specialists Conference, pp. 1384-1389, 1988.

[53] R.P. Gale, R.W. McClelland, B.D. Dingle, J.V. Gormley, R.M. Burgess, N.P. Kim, R.A. Mickelsen, and B.J. Stanbery, Conference record of 21st IEEE Photovoltaic Specialists Conference, pp. 53-57, 1990.

[54] R.W. Birkmire, L.C. DiNetta, J. Meakin, J.E. Phillips, Conference record of 17th IEEE Photovoltaic Specialists Conference, pp. 1406-1407, 1984.

[55] B.E. McCandless, R.W. Birkmire, W.A. Buchanan, J.E. Phillips, and R.E. Rocheleau, Conference record of 20th IEEE Photovoltaic Specialists Conference, pp. 381-384, 1988.

[56] M. Arienzo and J.J. Loferski, Conference record of 13th IEEE Photovoltaic Specialists Conference, pp. 898-903, 1978.

[57] K.L. Chopra and S.R. Das, Thin Film Solar Cells, New York, Plenum Press, pp. 505, 1983.

[58] W.H. Bloss, J. Kimmerle, F. Pfisterer, and H.W. Schock, Conference record of 17th IEEE Photovoltaic Specialists Conference, pp. 715-720, 1984.

[59] M.A. Contreras, J. Tuttle, A. Gabor, A. Tennant, K. Ramanathan, S. Asher, A. Franz, J. Keane, L. Wang, J. Scofield, and R. Noufi, First World Conference on Photovoltaic Energy Conference, 1994, pp. 68-75.

[60] W.H. Bloss, F. Pfisterer, M. Schubert, T. Walter, Progress in Photovoltaics, Vol. 3, pp. 3-24, 1995.

[61] K. Siemer, J. Klaer, I. Luck, J. Bruns, R. Klenk, D. Bräumig, Solar Energy Materials and Solar Cells, Vol. 67, pp. 159-166, 2001.

[62] T.M. Friedlmeier and H.W. Schock, Second World Conference on Photovoltaic Solar Energy Conversion, pp. 1117-1120, 1998.

[63] D. Lincot, R. Ortega-Borges, J. Vedel, M. Ruckh, J. Kessler, K. O. Velthaus, D. Hariskos, and H. W. Schock, 11th E. C. Photovoltaic Solar Energy Conference, p. 872, 1992.

[64] T. M. Friedlmeier, D. Braunger, D. Hariskos, M. Kaiser, H. N. Wanka, and H. W. Schock, Conference Record of the 25th IEEE PVSC, p. 845, 1996.

[65] Sheng S. Li, B. J. Stanbery, C. H. Huang, C. H. Chang, T. J. Anderson, and Y. S. Chang, Conference Record of the 25th IEEE Photovoltaic Specialists Conference, p. 821, 1996.

[66] Y.-S. Chang, Sheng S. Li, R. Datta, and L. P. Allen, Solid-State Electronics, Vol. 41, p. 1189, 1997.

[67] L. Ward, The Optical Constants of Bulk Materials and Films, Adam Hilger, England, 1988.

[68] M. Levy, E. Scheild, S. Cristoloveanu, and P. Hemment, Thin Solid Films, Vol. 148, p. 127, 1987.

[69] J. I. Pankove, Optical Process in Semiconductors, Dover, New York, 1975.

[70] Yun-Shan Chang and Sheng S. Li, Solid-State Electronics, 38(2), p. 297, 1995.

[71] K. Ramanathan, M. A. Contreras, J. R. Tuttil, J. Keane, J. Webb, S. Asher, D. Niles, R. Dhere, A. L. Tennant, F. S. Hasoon, and R. Noufi, Conference Record of the 25th IEEE Photovoltaic Specialists Conference, p. 837, 1996.

[72] S. Zott and K. Leo, Conference Record of the 25th IEEE Photovoltaic Specialists Conference, p. 817, 1996.

[73] J.R. Vig, J. Vac. Sci. Technol. A, Vol. 3, p. 1027, 1985.

[74] C.R. Osterwald, Solar Cells, Vol. 18, p. 269, 1986.

[75] A. Schönecker and K. Bücher, Conference Record of 22nd IEEE Photovoltaic Specialists Conference, pp. 203-208 1991.

[76] G. Sala, J. Olivan, and J.C. Zamorano, Proceedings of the 11th E.C. Photovoltaic Solar Energy Conference, pp. 341-343, 1992.

[77] T. Negami, Y. Hashimoto, and S. Nishiwaki, Solar Energy Materials and Solar Cells, Vol. 67, pp. 331-335 ,2001.

[78] E. Niemi, J. Hedstrom, T. Martinsson, K. Granath, L. Stolt, J. Skarp, D. Hariskos, M. Ruckh, H.W. Schock, Conference Record of the 25th IEEE Photovoltaic Specialists Conference, pp. 801-804, 1996.

[79] J. Kessler, K.O. Velthaus, M. Ruckh, R. Laichinger, H.W. Schock, D. Lincot, R. Ortega and J. Vedel, 6th Photovoltaic Science and Engineering Conference (PVSEC-6) Proceedings, New Delhi, India, pp. 1005-1010, 1992.

[80] K. Ramanathan, R.N. Bhattacharya, J. Granata, J. Webb, D. Niles, M.A. Contreras, H. Wiesner, F.S. Hasoon, and R. Noufi, Conference record of the 26th IEEE Photovoltaic Specialists Conference, p. 319, 1997.

[81] C.H. Huang, Sheng S. Li, W.N. Shafarman, C.-H. Chang, J.W. Johson, L. Reith, S. Kim, B.J. Stanbery, and T.J. Anderson, Technical Digest of the 11th International Photovoltaic Science and Engineering Conference, p. 855, 1999.

[82] T. Nakada, and M. Mizutani, Japanese Journal of Applied Physics, Part 2, Vol. 41, Issue 2B, pp. L165-L167, 2002.

[83] D. Hariskos, M. Ruckh, U. Rühle, T. Walter, H.W. Schock, J. Hedström, and L. Stolt, Solar Energy Materials and Solar Cells, Vol. 41/42, pp. 345-353, 1996.

[84] J.F. Moulder, W.F. Stickle, P.E. Sobol, and K.D. Bomben, Handbook of X-ray Photoelecttron Spectroscopy, pp. 45, 61, and 213-242, 1995.

[85] C. Heske, D. Eich, R. Fink, E. Umbach, T. van Buuren, C. Bostedt, L.J. Terminello, S. Kakar, M.M. Grush, T.A. Callcott, F.J. Himpsel, D.L. Ederer, R.C.C. Perera, W. Riedl, and F. Karg, Applied Physics Letters, Vol. 74, pp. 1451-1453, 1999.

[86] I. Luck, U. Störkel, W. Bohne, A. Ennaoui, M. Schmidt, H.W. Schock, and D. Bräunig, Thin Solid Films, Vol. 387, pp. 100-103, 2001.

[87] R. Bayon, C. Guillen, M.A. Martinez, M.T. Gutierrez, and J. Herrero, J. Electrochem. Soc., Vol. 145, pp. 2775-2779, 1998.

[88] C. -H. Chang, A. A. Morrone, B. J. Stanbery, C. McCreary, M. Huang, C. H. Huang, S. S. Li, and T. J. Anderson, AIP Conference Proceedings (NCPV Program Review Meeting), No. 462, pp. 114-119, 1998.

[89] R. Bayon, C. Maffiotte, and J. Herrero, Thin Solid Films, Vol. 353, pp. 100-107, 1999.

[90] M.A. Contreras, H. Wiesner, D. Niles, K. Ramanathan, R. Matson, J. Tuttle, J. Keane, and R. Noufi, Conference Record of the 25th IEEE Photovoltaic Specialists Conference, pp. 809-812, 1996.

[91] R. Herberhoz, U. Rau, H.W. Schock, T. Haalboom, T. Gödecke, F. Ernst, C. Beilharz, K.W. Benz, and Cahen, European Physical J. Appl. Phys, Vol. 6, pp. 131-139, 1999.

[92] J. Guillemoles, T. Haalboom, T. Gödecke, F. Ernst, D. Cahen, Mat. Res. Soc. Symp. Proc., 485, pp. 127-132, 1998.

[93] Hong Zhu, A.K. Kalkan, J. Hou, and S.J. Fonash, AIP Conference Proceedings, No. 462, pp. 309-314, 1999.

[94] S.H. Wei and Alex Zunger, J. Appl. Phys., Vol. 78, pp. 3846-3856, 1995.

[95] David J. Schroeder, Jose Luis Herberholz, and Angus A. Rockett, 11th Int. Conf. on Ternary and Multinary Compounds, pp. 749-752, 1999.

[96] G. Henna, A. Jasenek, U. Rau, and H.W. Schock, Thin Solid Films, Vol. 387, pp. 71-73, 2001.

[97] S.H. Wei, and S.B. Zhang, and A. Zunger, Applied Physics Letters, Vol. 72, pp. 3199-3201, 1998.

[98] T. Walter, R. Menner, M. Ruckh, L. Kaser, and H.W. Schock, Conference Record of the 22nd IEEE Photovoltaic Specialists Conference, pp. 924-929, 1991.

[99] T. Dullweber, G. Hanna, U. Rau, and H.W. Schock, Solar Energy Materials & Solar Cells, Vol. 67, pp.145-150, 2001.

[100] H. Kroemer, RCA Review, Vol. 18, pp. 332, 1957.

[101] F.S. Hasoon, Y. Yan, H. Althani, K.M. Jones, H.R. Moutinho, J. Alleman, M.M. Al-Jassim, and R. Noufi, Thin Solid Films, Vol. 387, pp. 1-5, 2001.

[102] F.S. Hasoon, H.A. Al-Thani, K.M. Jones, Y. Yan, H.R. Moutinho, M. Young, S.E. Asher, J. Alleman, R. Bhattacharya, K. Ramanathan, J. Keane, and M.M. Al-Jassim, Mat. Res. Soc. Symp. Proc., Vol. 668, pp. H6.8.1-7, 2001.

[103] L.C. Olsen, Wenhua Lei, F.W. Addis, W.N. Shafarman, M.A. Contreras, K. Ramanathan, Conference record of 26th IEEE Photovoltaic Specialists Conference, pp. 363-366, 1997.

[104] S. Chaisitsak, A. Yamada, M. Konagai, K. Saito, Japanese Journal of Applied Physics, Part 1, Vol. 39, no. 4, pp. 1660-1664, 2000.

[105] T. Nii, I. Sugiyama, T. Kase, M. Sato, Y. Kaniyama, S. Kuriyagawa, K. Kushiya, H. Takeshita, Conference record of the first world conference on Photovoltaic Solar Energy Conversion, pp. 254-257, 1994.

# BIOGRAPHICAL SKETCH

Chia-Hua Huang was born in Hualien, Taiwan, on March 16, 1967. He received the Bachelor of Science degree in the Department of Electrical Engineering from the National Sun Yat-Sen University, Taiwan, in 1991.

In August of 1995, he enrolled in the Department of Electrical and Computer Engineering at the University of Florida in Gainesville. He joined Professor Sheng S. Li's research laboratory in 1996. In December of 1997, he was awarded a Master of Science degree in Electrical and Computer Engineering from the University of Florida. After his graduation, he continued to work towards his Ph.D. degree. His research has been focused on the characterization and fabrication of CIS-based thin-film solar cells for the use of low-cost terrestrial power generation.

I certify that I have read this study and that in my opinion it conforms to acceptable standards of scholarly presentation and is fully adequate, in scope and quality, as a dissertation for the degree of Doctor of Philosophy.

ShengSan Li

Sheng S. Li, Chairman
Professor of Electrical and Computer Engineering

I certify that I have read this study and that in my opinion it conforms to acceptable standards of scholarly presentation and is fully adequate, in scope and quality, as a dissertation for the degree of Doctor of Philosophy.

Gijs Bosman
Professor of Electrical and Computer Engineering

I certify that I have read this study and that in my opinion it conforms to acceptable standards of scholarly presentation and is fully adequate, in scope and quality, as a dissertation for the degree of Doctor of Philosophy.

Arnost Neugroschel

Arnost Neugroschel
Professor of Electrical and Computer Engineering

I certify that I have read this study and that in my opinion it conforms to acceptable standards of scholarly presentation and is fully adequate, in scope and quality, as a dissertation for the degree of Doctor of Philosophy.

Timothy J. Anderson

Timothy J. Anderson
Professor of Chemical Engineering

This dissertation was submitted to the Graduate Faculty of the College of Engineering and to the Graduate School and was accepted as partial fulfillment of the requirements for the degree of Doctor of Philosophy.

August 2002

Pramod Khargonekar

Pramod P. Khargonekar
Dean, College of Engineering

Winfred M. Phillips
Dean, Graduate School